



1    **Dissimilar Roles of Aerosols, Nitrogen Deposition and Ozone on the Terres-  
2    trial Carbon Sink in China during 2010-2020**

3    **Nanhong Xie<sup>1</sup>, Tijian Wang<sup>1\*</sup>, Shu Li<sup>1</sup>, Bingliang Zhuang<sup>1</sup>, Mengmeng Li<sup>1</sup>, Min Xie<sup>2</sup>,**  
4    **Qian Zhang<sup>1</sup>, Danyang Ma<sup>2</sup>, Jane Liu<sup>3</sup>, Jing M. Chen<sup>3</sup>, Zhaozhong Feng<sup>4</sup>, Dimitrios Me-  
5    las<sup>5</sup>, Kostas Karatzas<sup>6</sup>**

6    <sup>1</sup>School of Atmospheric Sciences, Nanjing University, Nanjing, China

7    <sup>2</sup>School of Environment, Nanjing Normal University, Nanjing, China

8    <sup>3</sup>Department of Geography and Planning, University of Toronto, Toronto, Ontario, Canada

9    <sup>4</sup>Key Laboratory of Ecosystem Carbon Source and Sink, China Meteorological Administra-  
10    tion (ECSS-CMA), School of Ecology and Applied Meteorology, Nanjing University of In-  
11    formation Science and Technology, Nanjing, China

12    <sup>5</sup>Laboratory of Atmospheric Physics, School of Physics, Aristotle University of Thessaloniki,  
13    Thessaloniki, Greece

14    <sup>6</sup>Environmental Informatics Research Group, School of Mechanical Engineering, Aristotle  
15    University of Thessaloniki, Thessaloniki, Greece

16

17    *Corresponding to: Tijian Wang ([tjwang@nju.edu.cn](mailto:tjwang@nju.edu.cn))*

18

19    **Abstract**

20    China's Clean Air Action (CAA) plan implemented since 2013 has significantly altered atmos-  
21    pheric composition, and yet its impact on the terrestrial carbon sink remains unclear. This study  
22    employed the Regional Earth System Model (RegESM), an online-coupled climate–chemistry–  
23    ecosystem modeling framework, to quantify the impacts of aerosols, surface ozone ( $O_3$ ), and  
24    nitrogen deposition on China's net ecosystem productivity (NEP) from 2010 to 2020. The re-  
25    sults show that aerosols enhanced China's NEP by  $17.93 \text{ TgC yr}^{-1}$  (4.49% of the total NEP),  
26    primarily by increasing diffuse radiation, with the most pronounced effects in Southern and  
27    Eastern China. Nitrogen deposition further increased NEP by  $37.98 \text{ TgC yr}^{-1}$  (9.52%),



28 concentrated in Central and Southern regions. In contrast, O<sub>3</sub> pollution reduced NEP by 51.33  
29 TgC yr<sup>-1</sup> (12.9%), particularly in the forest-dominated Southeast. The positive impacts of aer-  
30 osols and nitrogen deposition on the carbon sink weakened over time, whereas the negative  
31 influence of O<sub>3</sub> was increasing. The combined effects indicate that CAA-induced atmospheric  
32 chemistry changes reversed the dominant atmospheric drivers of China's terrestrial carbon sink,  
33 from enhancement by aerosols and nitrogen deposition to suppression by ozone. Our findings  
34 highlight the need for stronger O<sub>3</sub> pollution control to achieve co-benefits between air-quality  
35 improvement and carbon neutrality.

36 **1 Introduction**

37 Terrestrial ecosystems act as major carbon sinks, sequestering atmospheric carbon dioxide  
38 (CO<sub>2</sub>) through plant photosynthesis, and constitute a fundamental natural process for mitigating  
39 global climate change (Friedlingstein et al., 2023; Piao et al., 2013; Yuan et al., 2025). Under  
40 ongoing global warming, the dynamics of carbon sinks are regulated not only by climatic fac-  
41 tors such as temperature and precipitation (Cao et al., 2023; Post et al., 2018; Ren et al., 2020),  
42 but also by variations in atmospheric composition (Zhou et al., 2021). Among these, aerosols,  
43 O<sub>3</sub>, and atmospheric nitrogen deposition have been identified as key atmospheric pollutants  
44 affecting terrestrial carbon sequestration (Liu et al., 2022; Zhou et al., 2024). As a crucial com-  
45 ponent of the global carbon cycle, terrestrial ecosystems in China sequester approximately  
46 0.20–0.25 PgC yr<sup>-1</sup>, playing an essential role in supporting the achievement of the national car-  
47 bon neutrality target (Piao et al., 2022; Xia et al., 2025; Yue et al., 2021). Therefore, assessing  
48 the responses of carbon sinks to multiple atmospheric composition changes is of great scientific  
49 significance for understanding both the global carbon cycle and climate feedback mechanisms.

50 Aerosols influence vegetation photosynthesis and carbon sequestration primarily through  
51 radiative forcing (Shu et al., 2022; Zhou et al., 2022). Aerosol scattering and absorption reduce  
52 surface solar radiation and can suppress vegetation photosynthesis (Doughty et al., 2010;  
53 Kuniyal and Guleria, 2019). In the meantime, enhanced diffuse radiation increases light use  
54 efficiency of plants, leading to the diffuse fertilization effect (Gu et al., 2003; Mercado et al.,  
55 2009). Aerosols also influence cloud microphysics by modifying droplet formation and lifetime,



56 which further affects regional precipitation and water availability for vegetation (Li et al., 2020;  
57 Unger et al., 2017). Consequently, the net effect of aerosols on photosynthesis exhibits marked  
58 spatial heterogeneity, with both enhancement and suppression reported in highly polluted re-  
59 gions such as eastern China (Strada and Unger, 2016; Wang et al., 2018; Xie et al., 2020).

60 In addition, near-surface O<sub>3</sub> impairs plant carbon uptake through direct physiological  
61 damage (Lei et al., 2022; Unger et al., 2020). O<sub>3</sub> enters leaves through stomata and induces  
62 reactive oxygen species at the cellular level, leading to degradation of photosynthetic pigments,  
63 suppressed Rubisco activity, premature leaf senescence, and defoliation, all of which inhibit  
64 photosynthetic carbon assimilation (Wittig et al., 2007). Evidence from O<sub>3</sub>-FACE (free-air O<sub>3</sub>  
65 concentration enrichment) experiments shows that a 10 ppb increase in O<sub>3</sub> concentration can  
66 lower crop productivity by 5–15% (Feng et al., 2015). In China, summertime O<sub>3</sub> peaks often  
67 coincide with the peak growing season of vegetation, particularly in the North China Plain and  
68 the Yangtze River Delta, posing a notable threat to regional carbon sequestration (Lei et al.,  
69 2022; Li et al., 2024; Yue et al., 2017).

70 Furthermore, atmospheric nitrogen deposition is a major external nitrogen source for ter-  
71 restrial ecosystems and exerts both positive and negative effects on carbon sinks (Chen et al.,  
72 2015; Lu et al., 2021). In nitrogen-limited systems, such as temperate forests and grasslands,  
73 moderate deposition can enhance photosynthesis and biomass accumulation, thereby increas-  
74 ing carbon sequestration (Cen et al., 2025; Lu et al., 2016; Peng et al., 2025). When inputs  
75 become excessive, however, they can induce soil acidification, biodiversity loss, and broader  
76 ecosystem degradation, a condition known as nitrogen saturation (Chen et al., 2015; Yue et al.,  
77 2016). China receives some of the highest nitrogen deposition levels globally, with annual av-  
78 erages of 15–20 kg N ha<sup>-1</sup> yr<sup>-1</sup> and hotspots surpassing 30 kg N ha<sup>-1</sup> yr<sup>-1</sup>, raising increasing  
79 concerns about long-term ecological impacts (Liu et al., 2022; Liu et al., 2013; Yu et al., 2019).

80 China has long faced the dual pressures of severe air pollution and growing greenhouse  
81 gas emissions (Tu et al., 2019; Wang et al., 2024). Rapid economic expansion in the early 2010s  
82 was accompanied by persistent increases in fine particulate matter (PM<sub>2.5</sub>) concentrations (Hao  
83 et al., 2020). Since 2013, successive Clean Air Action Plans have led to a substantial decline in  
84 PM<sub>2.5</sub> levels (Xue et al., 2019; Yue et al., 2020; Zheng et al., 2018). At the same time, near-



85 surface summertime O<sub>3</sub> has risen sharply (Liu et al., 2018; Zhou et al., 2024), while nitrogen  
86 deposition has slowed in growth but remains at a high level (Liu et al., 2024). These changes  
87 not only reflect the outcomes of emission control policies but also reshape the regional atmos-  
88 pheric chemical environment, potentially exerting complex and combined effects on carbon  
89 sinks (Liu et al., 2022; Zhou et al., 2024). The rapid transition in atmospheric composition  
90 during 2010–2020 provides an unprecedented large-scale natural experiment for disentangling  
91 the relative roles of aerosols, O<sub>3</sub>, and nitrogen deposition in altering China’s carbon sink. How-  
92 ever, most existing studies have examined these drivers in isolation, relied on offline or statis-  
93 tical frameworks that cannot capture dynamic climate–chemistry–ecosystem feedbacks, and  
94 rarely compared responses across ecological regions (Unger et al., 2020; Yue et al., 2017; Zhou  
95 et al., 2024).

96 Here, we employ an improved regional climate–chemistry–ecosystem online-coupling  
97 model, RegESM (Xie et al., 2024; Zhang et al., 2025), to quantify the impacts of aerosols, O<sub>3</sub>,  
98 and nitrogen deposition on China’s terrestrial carbon sinks during 2010–2020. RegESM incor-  
99 porates two-way interactions among climate, atmospheric chemistry, and biogeochemical pro-  
100 cesses and has been extensively evaluated over East Asia (Ma et al., 2023; Xie et al., 2024; Xie  
101 et al., 2020; Zhang et al., 2025). Our objective is to isolate the contributions of individual at-  
102 mospheric components to changes in China’s carbon sinks based on RegESM after its assess-  
103 ment using multiple observational datasets. These results offer new insight into the ecological  
104 consequences of rapid atmospheric composition changes and provide a scientific foundation  
105 for coordinated multi-pollutant control and ecosystem management under China’s carbon-neu-  
106 trality goals.

## 107 **2 Data and Methods**

### 108 **2.1 The RegESM model**

109 In this study, we employed the RegESM, an improved extension of the RegCM-Chem-  
110 YIBs regional climate–chemistry–ecosystem modeling framework (Xie et al., 2024; Xie et al.,  
111 2019; Zhang et al., 2025). The original RegCM-Chem-YIBs couples the RegCM4 regional



112 climate model (Giorgi et al., 2012), the radiative interactive gas-phase chemistry module Chem  
113 (Shalaby et al., 2012), and the YIBs terrestrial ecosystem model (Yue and Unger, 2015) to  
114 represent interactive processes among atmospheric dynamics, chemistry, and terrestrial carbon  
115 cycles (Xie et al., 2024). Building upon this foundation, RegESM strengthens two-way feed-  
116 back among the atmosphere, atmospheric chemistry, and land surface processes, enabling a  
117 more realistic simulation of biogeochemical cycles (Zhang et al., 2025). The enhanced coupling  
118 allows land surface changes, such as vegetation dynamics and soil moisture variations, to more  
119 directly influence atmospheric composition, radiation, and meteorology, while atmospheric  
120 and chemical variations simultaneously affect ecosystem processes (Xie et al., 2024; Zhang et  
121 al., 2025). This bidirectional integration improves the model's capability to capture transient  
122 and spatially heterogeneous climate–ecosystem–chemistry interactions, which are crucial for  
123 regional climate change and carbon budget assessments (Zhang et al., 2025).

124 The RegESM framework used in this study integrates RegCM4 as the dynamical core for  
125 simulating regional climate processes at a high resolution, the Chem module for interactive  
126 gas-phase and aerosol chemistry coupled with radiation and meteorology, and the YIBs land  
127 surface model for calculating biophysical processes such as photosynthesis, transpiration, and  
128 energy balance, along with biogeochemical cycles of carbon and nitrogen (Giorgi et al., 2012;  
129 Shalaby et al., 2012; Xie et al., 2024; Yue and Unger, 2015). These components are linked  
130 through an improved coupling mechanism that ensures the consistent exchange of meteorolog-  
131 ical, chemical, and biogeophysical variables at each model timestep, enabling fully interactive  
132 simulations in which land, atmosphere, and chemistry evolve in a physically coherent manner  
133 (Xie et al., 2024; Zhang et al., 2025). This model has been widely applied in East Asia (Xie et  
134 al., 2025; Xie et al., 2019; Zhang et al., 2025; Zhang et al., 2024).

135 We used net ecosystem productivity (NEP) as an indicator for characterizing carbon  
136 sources and sinks (NEP > 0 suggests a carbon sink). NEP was calculated as the difference  
137 between gross primary production (GPP) and the sum of autotrophic respiration (Ra) and het-  
138 erotrophic respiration (Rh) (Xie et al., 2025; Yue et al., 2021). It is noteworthy that the NEP  
139 estimated in this study does not account for lateral carbon transfers.

140 **2.2 Ozone Damage Scheme**



141 Once surface O<sub>3</sub> enters plants through the stomata, it directly damages plant cellular struc-  
142 tures and suppresses the photosynthetic rate, thereby reducing vegetation productivity. In the  
143 YIBs vegetation module of the RegESM model, a semi-mechanistic parameterization scheme  
144 is employed to represent the impacts of O<sub>3</sub> on plants (Sitch et al., 2007; Yue and Unger, 2015):

145 
$$B = B_{tot} \cdot K, \quad (1)$$

146 where B denotes the photosynthetic rate under O<sub>3</sub> exposure,  $B_{tot}$  represents the total leaf pho-  
147 tosynthetic rate, and K is the remaining proportion of photosynthetic capacity after O<sub>3</sub> stress.  
148 This proportion is determined by the stomatal O<sub>3</sub> flux that exceeds a specified threshold:

149 
$$K = 1 - b \cdot \max[(K_{ozn} - K_{ozncrit}), 0], \quad (2)$$

150 where b denotes the vegetation sensitivity parameter to O<sub>3</sub> derived from observational data.  
151  $K_{ozncrit}$  represents the threshold of O<sub>3</sub>-induced damage to vegetation, and  $K_{ozn}$  denotes the  
152 O<sub>3</sub> flux entering the leaf through stomata:

153 
$$K_{ozn} = \frac{[O_3]}{r_b + \frac{\kappa_{O3}}{r_s}}, \quad (3)$$

154 where [O<sub>3</sub>] denotes the O<sub>3</sub> concentration at the canopy top,  $r_b$  is the boundary layer resistance,  
155  $\kappa_{O3}$  is the ratio of O<sub>3</sub> leaf resistance to water vapor blade resistance, and  $r_s$  is the stomatal  
156 resistance accounting for the effects of O<sub>3</sub>:

157 
$$r_s = g_s \cdot K. \quad (4)$$

158  $g_s$  denotes the leaf conductance unaffected by O<sub>3</sub> exposure. By simultaneously solving Equa-  
159 tions (2), (3), and (4), a quadratic term with respect to K is obtained, which can be solved  
160 analytically.

161 **2.3 Experimental design and input data**

162 The simulation domain covers most of East Asia (Fig. S1), centered at 36° N and 107° E.  
163 The horizontal resolution is 30 km, with 18 vertical layers. To quantify the independent con-  
164 tributions of aerosol, O<sub>3</sub> damage, and atmospheric nitrogen deposition to China's terrestrial  
165 carbon sink during 2010–2020, four sensitivity experiments were conducted (Table 1): a base-  
166 line simulation without these effects (Base), and three single-factor cases that enabled only  
167 aerosol (Ctrl\_AOD), O<sub>3</sub>-induced vegetation damage (Ctrl\_O<sub>3</sub>), and nitrogen deposition



168 impacts (Ctrl\_Ndep). The difference between each sensitivity case and the Base run represents  
169 the corresponding individual effect. All simulations were preceded by a one-year spin-up to  
170 reduce the influence of initial conditions. To further assess regional responses, China was di-  
171 vided into six representative subregions (Fig. S2), and statistical analyses were performed for  
172 each.

173

174 **Table 1.** Numerical model experiments.

Simulations	Periods	Aerosol radiative effect	O <sub>3</sub> damage	atmospheric nitrogen deposition
Base	2010-2020	off	off	off
Ctrl_AOD	2010-2020	open	off	off
Ctrl_O <sub>3</sub>	2010-2020	off	open	off
Ctrl_Ndep	2010-2020	off	off	open

175

176 The initial and boundary meteorological fields were taken from the ECMWF (European  
177 Centre for Medium-Range Weather Forecasts) ERA-Interim reanalysis with a temporal reso-  
178 lution of 6 h and a horizontal resolution of 1.5° × 1.5° (Hersbach et al., 2020). Aerosol initial  
179 and boundary conditions were provided by the global chemical transport model (MOZART)  
180 (Emmons et al., 2010; Horowitz et al., 2003). Background CO<sub>2</sub> fields were constrained by  
181 three-dimensional concentrations from NOAA CarbonTracker (CT) reanalysis (Peters et al.,  
182 2007). The initial parameters for the YIBs model were derived from soil carbon stocks based  
183 on equilibrium tree height and a 30-year harvest cycle (Yue and Unger, 2015). Vegetation  
184 cover was prescribed from MODIS and AVHRR (Advanced Very High Resolution Radiometer)  
185 datasets (Lawrence and Chase, 2007). Anthropogenic emissions in China were taken from the  
186 Multi-resolution Emission Inventory for China (MEIC) (Geng et al., 2024; Li et al., 2017;  
187 Zheng et al., 2018).

188 **2.4 Validation data**



189 We employed monthly mean aerosol optical depth (AOD) data from the MODIS sensor  
190 onboard NASA's Terra satellite (MOD08\_M3.061). The data have a spatial resolution of  $1^\circ \times$   
191  $1^\circ$  and are retrieved using three algorithms: the Dark Target, Deep Blue, and combined ap-  
192 proaches (Levy et al., 2013). Ground-level O<sub>3</sub> observations were obtained from 366 monitoring  
193 stations operated by the China National Environmental Monitoring Center (CNEMC). To eval-  
194 uate the model's capability in simulating atmospheric nitrogen deposition, we employed pub-  
195 licly available datasets (Liu et al., 2024; Zhu et al., 2025). These datasets integrate observations  
196 with model outputs to provide nitrogen deposition estimates at both global and regional scales  
197 over China. To assess the reliability of simulated CO<sub>2</sub>, we used observations from the World  
198 Data Centre for Greenhouse Gases (WDCGG). This dataset provides measured surface atmos-  
199 pheric CO<sub>2</sub> concentrations and was used to evaluate the model's ability to reproduce observed  
200 CO<sub>2</sub> levels. For the spatial distribution of CO<sub>2</sub>, we additionally used CO<sub>2</sub> concentration fields  
201 from CT (Peters et al., 2007). For GPP and net primary production (NPP) validation, we used  
202 the global MODIS products MOD17A2H and MOD17A3H (Collection 6). The GPP data, at  
203 8-day resolution, were derived using the radiation use efficiency algorithm, while NPP  
204 (NPP=GPP-Ra) data were produced by annually accumulating GPP values, with a spatial res-  
205 olution of 500 m (He et al., 2018; Madani et al., 2014).

206 **2.5 Analytical Approach**

207 Aerosol-induced meteorological changes are highly interdependent, making it challenging  
208 to isolate their individual effects on terrestrial carbon cycling. To quantify the relative contri-  
209 butions of these meteorological responses to vegetation carbon fluxes, we applied a multiple  
210 linear regression framework. Standardized regression coefficients were used to assess the rel-  
211 ative influence of each climate variable. This approach has been widely demonstrated as effec-  
212 tive for disentangling the impacts of multiple environmental drivers on ecosystem processes  
213 (Jung et al., 2017; Xie et al., 2025; Zhang et al., 2024).

214 The regression model is expressed as follows:

$$215 \Delta Y = A_1 \times \Delta X_1^{RadD} + A_2 \times \Delta X_2^{RadF} + A_3 \times \Delta X_3^{Temp} + A_4 \times \Delta X_4^{Precip} + A_5 \times \Delta X_5^{VPD} \\ 216 + \varepsilon \quad (5)$$



217 where  $\Delta Y$  denotes the difference in terrestrial carbon flux between the simulations Base and  
218 Ctrl\_AOD, respectively.  $\Delta X_1^{RadD}$ ,  $\Delta X_2^{RadF}$ ,  $\Delta X_3^{Temp}$ ,  $\Delta X_4^{Precip}$  and  $\Delta X_5^{VPD}$  denote  
219 the differences in direct radiation, diffuse radiation, temperature, precipitation, and vapor pres-  
220 sure deficit (VPD) between the simulations Base and Ctrl\_AOD, respectively.  $A_i$  represents  
221 the partial regression coefficient for different meteorological factors, indicating the sensitivity  
222 of carbon flux to variations in these factors.  $\varepsilon$  is the residual term of the regression model. We  
223 use the following equation to calculate the standardized regression coefficient  $B_i$  for compar-  
224 ing the relative impacts of different meteorological factors:

225 
$$B_i = A_i \times SD(\Delta X_i) \div SD(\Delta Y) \quad (6)$$

226 where  $SD(\Delta X_i)$  and  $SD(\Delta Y)$  represent the standard deviations of the changes in each mete-  
227 orological factor and carbon flux, respectively.  $B_i$  quantifies the relative contribution of dif-  
228 ferent meteorological factors to variations in carbon flux. This approach enables a quantitative  
229 assessment of the individual impacts of changes in each meteorological factor induced by aer-  
230 osol radiative effects on terrestrial carbon flux.

231 **3 Results**

232 **3.1 Model validations**

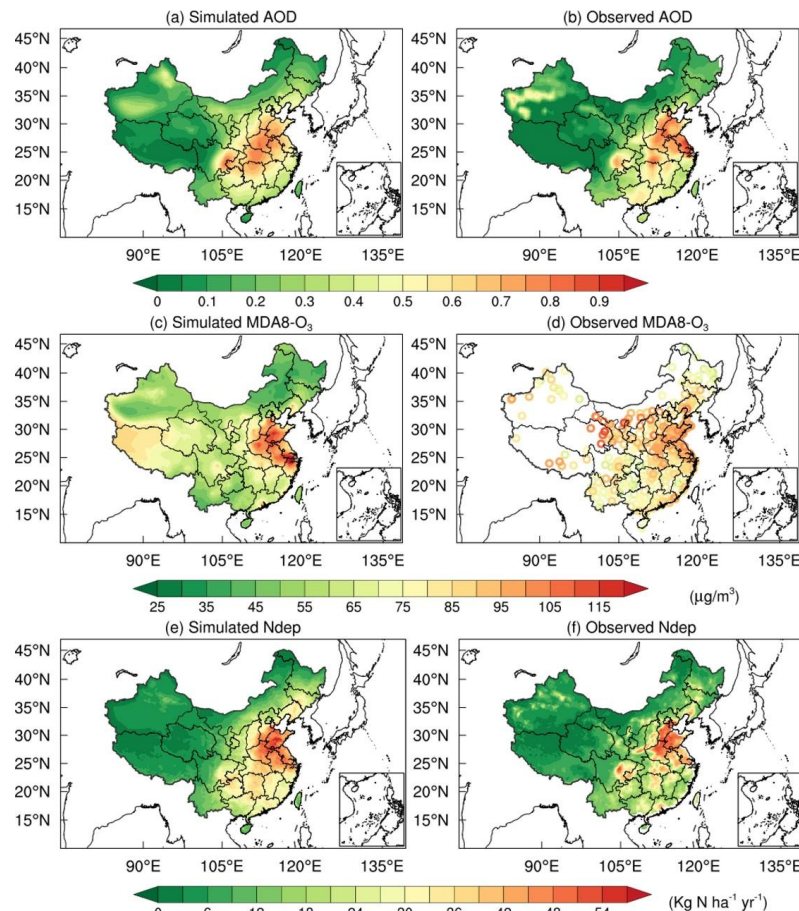
233 **3.1.1 Aerosols, surface ozone, and atmospheric nitrogen deposition**

234 We assessed the RegESM performance by comparing the 2010–2020 simulations with  
235 multi-source observations. Simulated AOD showed good agreement with MODIS products in  
236 both spatial distribution and magnitude (Fig. 1a, b). High AOD values are located over the  
237 North China Plain and the Sichuan Basin, consistent with dense anthropogenic emissions in  
238 these regions (Luo et al., 2014). The observations indicate that the national mean AOD de-  
239 creased from 0.36 in 2010 to 0.28 in 2020, driven by air quality improvement policies. We  
240 calculated statistical metrics, including the correlation coefficient (R), mean bias (MB), and  
241 root mean square error (RMSE), to evaluate the model performance (Fig. S3). The RegESM  
242 captures this trend with a correlation coefficient (R) of 0.71. However, compared with monthly  
243 MODIS AOD, the model shows a minor underestimation (MB = -0.02), which can be



244 attributed primarily to uncertainties in the anthropogenic emission inventories (Xie et al., 2020).  
245 Surface O<sub>3</sub> simulations reproduce both spatial patterns (Fig. 1c, d). The correlation with site  
246 observations reaches 0.72 (Fig. S4). High concentrations in the North China Plain, the Yangtze  
247 River Delta, and the Sichuan Basin are captured well, highlighting the model's skill in simu-  
248 lating O<sub>3</sub> fields. The simulated annual mean atmospheric nitrogen deposition flux ranges from  
249 20 to 40 kg N ha<sup>-1</sup> yr<sup>-1</sup> in eastern agricultural and urban areas, consistent with reported values  
250 of 25–35 kg N ha<sup>-1</sup> yr<sup>-1</sup> (Fig. 1e, f). The simulated national mean of 15.09 kg N ha<sup>-1</sup> yr<sup>-1</sup> is close  
251 to the dataset range of 13.45–15.39 kg N ha<sup>-1</sup> yr<sup>-1</sup>. The model also reproduces the observed  
252 decline after the implementation of air pollution control policies in 2013, with a gradual de-  
253 crease after 2015 (Fig. S5). These evaluations indicate that RegESM reliably simulates AOD,  
254 O<sub>3</sub>, and nitrogen deposition fields across China.

255



256

257 **Figure 1.** Annual mean AOD (a, b), maximum daily 8 h average (MDA8) O<sub>3</sub> (c, d), and At-  
258 mospheric nitrogen deposition (e, f) from model simulation (a, c, e) and observations (b, d, f).

259

### 260 **3.1.2 Atmospheric CO<sub>2</sub> concentrations, GPP, and NPP**

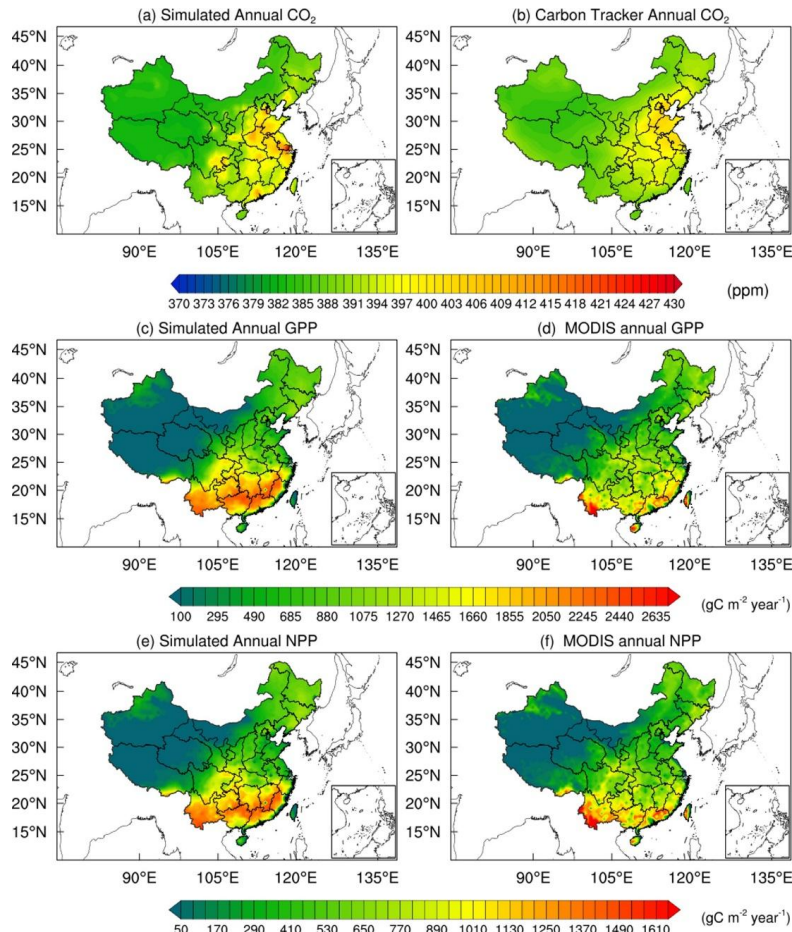
261 Simulated CO<sub>2</sub> concentrations were compared with six stations from the WDCGG. The  
262 correlation coefficients range from 0.83 to 0.96 (Table S1). The YON site shows the best agree-  
263 ment ( $R = 0.96$ ,  $MB = -1.1$  ppm), likely due to minimal influence from terrestrial emissions.  
264 In contrast, HKG and HKO show larger biases, with overestimates of 3.1 ppm ( $R = 0.83$ ) and  
265 3.3 ppm ( $R = 0.84$ ), probably linked to unaccounted variability in urban sources in monthly



266 inventories. Nevertheless, the seasonal cycle is reproduced well at all sites (Fig. S6).

267 We further compared simulated CO<sub>2</sub> with the CarbonTracker CT2022 assimilation dataset  
268 (Peters et al., 2007). The spatial correlation coefficient reaches 0.72 (Fig. 2a, b). High CO<sub>2</sub>  
269 concentrations appear over the Beijing–Tianjin–Hebei region, the Yangtze River Delta, the  
270 Pearl River Delta, and the Sichuan Basin, consistent with intense industrial emissions. The  
271 model slightly overestimates values in the Pearl River Delta, likely due to underrepresented  
272 local sources and complex topography. Overall, RegESM effectively captures the spatial dis-  
273 tribution of CO<sub>2</sub> concentrations.

274 Simulated GPP agrees well with MODIS in spatial distribution (Fig. 2c, d), with a spatial  
275 correlation of 0.89. However, GPP from this study is larger than MODIS GPP by 7.4%, with  
276 largest differences in Central (11.6%) and Southeast China (5.7%). Other studies also found  
277 that MODIS GPP was underestimated at high values (Xie et al., 2019; Zhang et al., 2012). The  
278 southeast-to-northwest decreasing gradient is reproduced, with high values over regions dom-  
279 inated by forest ecosystems. The seasonal cycle of GPP is also captured (Fig. S7). The simu-  
280 lated NPP exhibits a spatial distribution consistent with the MODIS (Fig. 2e, f), with a spatial  
281 correlation coefficient of 0.86. Similar to GPP, the model overestimates NPP by 8.4%, mainly  
282 due to the overestimation in Central (14.3%) and Northeastern (6.2%) China. These results  
283 confirm the model's ability to represent terrestrial carbon fluxes.



284

285 **Figure 2.** Annual mean CO<sub>2</sub> (a, b), GPP (c, d), and NPP (e, f) from model simulation (a, c, e)

286 and observations (b, d, f).

287

### 288 **3.2 Impacts of Aerosols on Meteorology and Carbon Sinks**

#### 289 **3.2.1 Impacts of Aerosols on Meteorological Factors**

290 During 2010–2020, the aerosol exerted a substantial influence on China’s surface radia-  
291 tion and near-surface climate (Fig. 3). Nationally, aerosols reduced downward direct solar ra-  
292 diation by  $8.81 \text{ W m}^{-2}$ , while increasing diffuse radiation by  $3.04 \text{ W m}^{-2}$ , leading to an overall  
293 reduction of  $5.77 \text{ W m}^{-2}$  in total shortwave radiation reaching the surface. Spatially, these



294 radiative changes were most pronounced over major urban agglomerations such as the North  
295 China Plain, the Yangtze River Delta, and the Sichuan Basin, coinciding with regions of high  
296 AOD associated with intensive anthropogenic emissions. These results are consistent with pre-  
297 vious modeling and satellite-based analyses (Wang et al., 2017; Xie et al., 2020), confirming  
298 the robustness of the simulated radiative forcing patterns.

299 The reduction in surface solar radiation directly perturbed the regional energy balance and  
300 atmospheric thermodynamics, resulting in a cooling effect over most of eastern and central  
301 China. As shown in Fig. 3d, surface air temperature decreased significantly in the Sichuan Ba-  
302 sin and coastal regions, with local maxima reaching  $-1.1^{\circ}\text{C}$ . In contrast, western and north-  
303 eastern China experienced weaker changes, consistent with lower AOD levels. The simulated  
304 national mean temperature decline of  $0.32^{\circ}\text{C}$  agrees well with previous RegCM-based studies  
305 (Wang et al., 2015; Xie et al., 2020). This widespread cooling is primarily attributed to aerosol-  
306 induced dimming, which suppresses surface shortwave absorption and weakens boundary-  
307 layer turbulence, thereby inhibiting vertical heat exchange and reducing near-surface tempera-  
308 tures.

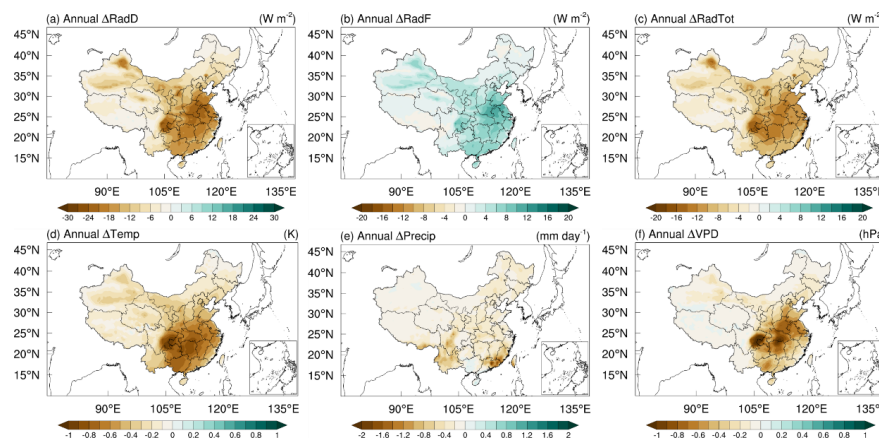
309 Aerosol also exerted a marked influence on regional hydrological processes. Precipitation  
310 decreased across much of southern and southwestern China, with notable reductions in Guang-  
311 dong, Fujian, Yunnan, and Sichuan provinces, where daily rainfall decreased by up to  $2\text{ mm}$   
312  $\text{day}^{-1}$  (Fig. 3e). On average, national precipitation declined by  $0.23\text{ mm day}^{-1}$ . The reduction in  
313 rainfall reflects the combined effects of radiative cooling and weakened convective activity.  
314 Specifically, aerosol-induced surface dimming stabilizes the lower atmosphere and suppresses  
315 the upward transport of moisture, while reduced latent heating further limits convective cloud  
316 formation. These mechanisms together explain the widespread drying observed in the simula-  
317 tions.

318 The VPD, a key indicator of plant water stress, also responded sensitively to aerosol forc-  
319 ing. As shown in Fig. 3f, aerosols significantly reduced VPD over central and southeastern  
320 China, with decreases of  $-0.3$  to  $-0.6\text{ hPa}$ , and locally up to  $-1.2\text{ hPa}$  in Sichuan, Hebei, and  
321 Jiangsu. The national mean reduction was  $-0.11\text{ hPa}$ . Lower VPD values imply a moister near-  
322 surface environment and weaker atmospheric demand for evapotranspiration. Ecologically, this



323 alleviation of plant water stress can enhance stomatal conductance and facilitate photosynthetic  
324 carbon uptake, thereby partially compensating for the productivity loss caused by reduced solar  
325 radiation. Thus, the aerosol-induced decline in VPD represents an important indirect pathway  
326 through which aerosols modulate the terrestrial carbon cycle, linking atmospheric radiative  
327 forcing to ecosystem function.

328



329 **Figure 3.** Annual mean changes in meteorological variables due to aerosol direct radiative  
330 effect during 2010–2020. (a) RadD, direct radiation; (b) RadF, diffuse radiation; (c) RadTot,  
331 total radiation; (d) Temp, air temperature; (e) Precip, precipitation; (f) VPD, vapor pressure  
332 deficit.

334

### 335 **3.2.2 Effects of Aerosols on the Terrestrial Carbon Sink**

336 During 2010–2020, the aerosol overall enhanced the productivity of China's terrestrial  
337 ecosystems, increasing GPP and NEP by  $293.28 \text{ TgC yr}^{-1}$  and  $17.93 \text{ TgC yr}^{-1}$ , accounting for  
338 3.98% and 4.49% of the national totals, respectively. Spatially, the responses of GPP and NEP  
339 to the aerosol radiative effect displayed significant heterogeneity, with pronounced enhance-  
340 ments in southern and eastern China (Fig. 4a, b). The most significant enhancements occurred  
341 in South-Central and East China, where GPP increased by  $0.32 \text{ gC m}^{-2} \text{ day}^{-1}$  and  $0.31 \text{ gC m}^{-2}$   
342  $\text{day}^{-1}$ , respectively. These regions are characterized by dense forests and cropland ecosystems  
343 with high leaf area index, enabling them to fully exploit the additional diffuse radiation induced



344 by aerosols. Meanwhile, the high aerosol loading in these regions ensured sufficient radiative  
345 perturbation, amplifying the improvement in canopy light-use efficiency. In the Southwest, the  
346 response was more complex. Although the mean GPP increased by  $0.20 \text{ gC m}^{-2} \text{ day}^{-1}$ , parts of  
347 Yunnan showed a negative effect. This reduction likely results from excessive attenuation of  
348 solar radiation under the region's unique topographic and climatic conditions, which con-  
349 strained photosynthetic activity. Nevertheless, NEP in this region remained positive (approxi-  
350 mately  $0.01 \text{ gC m}^{-2} \text{ day}^{-1}$ ), suggesting that the cooling effect of aerosols substantially sup-  
351 pressed ecosystem respiration, thereby compensating for the reduced photosynthesis. In con-  
352 trast, the North and Northwest exhibited weak positive responses ( $<0.07 \text{ gC m}^{-2} \text{ day}^{-1}$ ), while  
353 the Northeast showed slight inhibition ( $-0.04 \text{ gC m}^{-2} \text{ day}^{-1}$ ), probably due to aerosol-induced  
354 cooling delaying the onset of the growing season. Overall, the spatial patterns of GPP and NEP  
355 responses to the aerosol radiative effect show a clear latitudinal gradient: the humid, high-bio-  
356 mass ecosystems in southern and eastern China are most sensitive to diffuse radiation enhance-  
357 ment, whereas the high-latitude and arid regions experience limited or even negative responses  
358 due to temperature and radiation constraints.

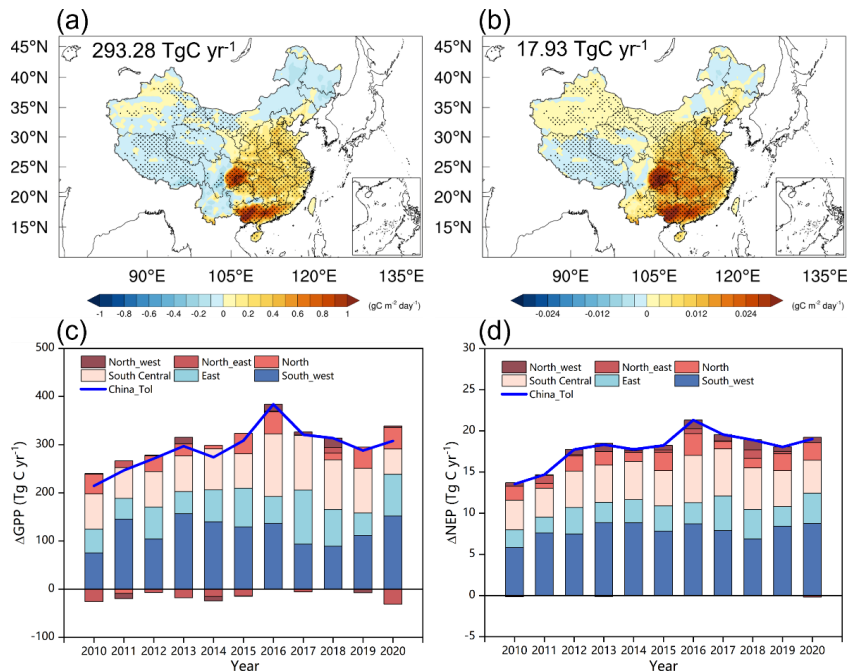
359 From 2010 to 2020, the influence of aerosols on carbon fluxes exhibited distinct interan-  
360 nual variability (Fig. 4c, d). Both GPP and NEP showed an upward trend before 2016, with  
361 GPP increasing from  $214.66 \text{ TgC yr}^{-1}$  in 2010 to  $384 \text{ TgC yr}^{-1}$  in 2016, and NEP rising from  
362  $13.54 \text{ TgC yr}^{-1}$  to  $21.31 \text{ TgC yr}^{-1}$ . The synchronous growth of GPP and NEP indicates that the  
363 aerosol radiative effect enhanced terrestrial carbon uptake mainly through photosynthetic ac-  
364 tivity. The strong enhancement during 2015–2017 coincided with years of high aerosol loading  
365 and a greater proportion of diffuse radiation, which improved canopy light-use efficiency under  
366 humid and cloudy conditions. After 2018, the positive effect weakened slightly and stabilized  
367 at a lower level. This reduction likely reflects the combined influence of cleaner atmospheric  
368 conditions and changing meteorological patterns, including increased direct radiation and a  
369 reduced diffuse fraction. Year-to-year variations were further modulated by hydroclimatic con-  
370 ditions: higher humidity and cloud cover enhanced aerosol scattering efficiency, while drier or  
371 cleaner years favored direct radiation and weakened the diffuse light advantage. Moreover, the  
372 smaller NEP fluctuations compared to GPP imply a delayed response of ecosystem respiration,



373 as aerosol-induced cooling moderates' respiration more gradually than photosynthesis. Overall,  
374 the interannual variability of GPP and NEP responses to the aerosol radiative effect highlights  
375 the coupled influences of aerosol loading, radiation balance, and regional climate variability  
376 on China's terrestrial carbon sink dynamics.

377 The effects of aerosols on GPP and NEP show pronounced seasonal variation (Fig. S8),  
378 driven by the dynamic coupling between vegetation phenology and environmental factors. In  
379 spring (March–May), aerosols increase GPP by 42.35 TgC (14.4%) and NEP by 2.82 TgC  
380 (15.7%), making a notable contribution at the start of the growing season as rising temperatures  
381 and rapid canopy expansion enhance diffuse radiation benefits, improving light-use efficiency;  
382 meanwhile, moderate cooling suppresses respiration without causing thermal stress, further  
383 boosting NEP. In summer (June–August), positive effects peak, with GPP rising by 173.62 TgC  
384 (59.2%) and NEP by 10.15 TgC (56.6%); under high solar radiation and full canopy closure,  
385 diffuse light penetration reaches its maximum, while cooling alleviates heat stress and reduces  
386 respiration, driving NEP to its annual maximum. In autumn (September–November), aerosols  
387 add 88.38 TgC to GPP (30.1%) and 3.95 TgC to NEP (22.0%), effectively extending the pho-  
388 tosynthetic period as shorter days and reduced total radiation increase the proportion of diffuse  
389 light, sustaining carbon storage. In winter (December–February), GPP declines slightly (-  
390 11.07 TgC, -3.8%), but NEP shows a small positive gain (1.01 TgC, 5.6%) because cooling  
391 strongly suppresses respiration, offsetting reduced photosynthesis. Overall, aerosol radiative  
392 effects regulate seasonal carbon cycling by modifying radiation and thermal conditions. The  
393 net impact depends on the trade-off between the fertilization effect of diffuse radiation and the  
394 opposing effects of reduced total radiation and cooling. Summer emerges as the primary driver  
395 of the annual net positive effect. Accurately quantifying this seasonal dynamic is crucial for  
396 assessing the ecological and climatic consequences of anthropogenic aerosols.

397



398 **Figure 4.** Spatiotemporal variations in carbon flux changes caused by the aerosol radiative  
399 effect during 2010–2020. (a–b) Multi-year mean spatial patterns of GPP and NEP changes  
400 caused by the aerosol radiative effect. National totals are shown in each panel. Black dots de-  
401 note significant changes ( $p < 0.01$ ). (c–d) Interannual variations of GPP and NEP changes  
402 caused by the aerosol radiative effect.

404

#### 405 **3.2.3 Contributions of Meteorological Factors to Carbon Sink Changes**

406 We quantified the independent contributions of aerosol-induced meteorological changes  
407 to carbon fluxes using the multiple linear regression analysis described in Section 2.5 (Fig. 5a,  
408 b). Overall, aerosol substantially influenced China's terrestrial carbon uptake by altering radi-  
409 ation composition and meteorological conditions. At the national scale, the increase in diffuse  
410 radiation emerged as the dominant positive driver, contributing to GPP ( $325.07 \text{ TgC yr}^{-1}$ ) and  
411 NEP ( $11.46 \text{ TgC yr}^{-1}$ ). This highlights the crucial role of the diffuse radiation fertilization effect,  
412 particularly in regions with high aerosol loading across eastern and southwestern China, where  
413 enhanced diffuse light improves canopy light distribution and photosynthetic efficiency. In



414 contrast, the reduction in direct radiation suppressed GPP (94.78 TgC yr<sup>-1</sup>) and NEP (2.59 TgC  
415 yr<sup>-1</sup>) due to insufficient illumination, though the impact on NEP was weaker, reflecting partial  
416 offset by the reduction in ecosystem respiration under aerosol-induced cooling. Cooling alone  
417 reduced GPP by 59.62 TgC yr<sup>-1</sup> and NEP by 4.73 TgC yr<sup>-1</sup>. This decline in NEP occurred  
418 because the decrease in GPP (driven by reduced transpiration and stomatal conductance) out-  
419 weighed the concurrent reduction in ecosystem respiration. Meanwhile, lower VPD enhanced  
420 GPP by 114.44 TgC yr<sup>-1</sup> and NEP by 8.25 TgC yr<sup>-1</sup> by alleviating water stress, reinforcing  
421 photosynthetic carbon uptake. Changes in precipitation played only a minor role, slightly re-  
422 ducing GPP (8.17 TgC yr<sup>-1</sup>) and NEP (0.62 TgC yr<sup>-1</sup>), with limited influence even in the mon-  
423soon regions of southern China. These findings indicate that variations in radiation components,  
424 rather than hydrometeorological perturbations, serve as the primary pathway through which  
425 aerosols modulate terrestrial carbon sinks.

426 Regionally, among these factors, diffuse radiation exerted the strongest positive influence  
427 on GPP across all regions, particularly in the southwest (115.92 TgC yr<sup>-1</sup>), east (67.04 TgC yr<sup>-1</sup>),  
428 and south-central (93.08 TgC yr<sup>-1</sup>) China (Fig. 5a, b). Enhanced diffuse light under elevated  
429 aerosol loading improved the vertical distribution of photosynthetically active radiation within  
430 the canopy and increased photosynthetic efficiency. In contrast, direct radiation consistently  
431 exhibited negative effects, most evident in the southwest (-42.32 TgC yr<sup>-1</sup>) and east (-22.92  
432 TgC yr<sup>-1</sup>), indicating that aerosol-induced solar dimming partly offset the diffuse radiation fer-  
433tilization benefit. Temperature changes associated with aerosol cooling suppressed GPP na-  
434 tionwide, especially in the southwest (-29.07 TgC yr<sup>-1</sup>) and south-central regions (-16.19 TgC  
435 yr<sup>-1</sup>), by lowering canopy temperature and reducing evapotranspiration. The contributions of  
436 precipitation were minor (-1 to -3 TgC yr<sup>-1</sup>), while VPD exerted a positive effect, particularly  
437 in humid southern regions (55.76 TgC yr<sup>-1</sup> in the southwest), suggesting that aerosol-induced  
438 cooling and moistening alleviated water stress and indirectly promoted carbon uptake. For NEP,  
439 diffuse radiation remained the dominant positive driver, with the largest increases in the south-  
440 west (4.06 TgC yr<sup>-1</sup>) and south-central (3.35 TgC yr<sup>-1</sup>) China, while direct radiation continued  
441 to exert negative effects. The temperature effect was moderate but consistent with GPP,



442 implying that aerosol cooling simultaneously suppressed photosynthesis and respiration, with  
443 a net positive outcome for NEP. Taken together, these spatial contrasts highlight the combined  
444 effects of aerosol composition, vegetation structure, and regional hydroclimate, emphasizing  
445 that radiative forcing dominates in humid, high-biomass ecosystems, whereas climatic con-  
446 straints prevail in arid zones.

447 To further clarify the dominant controls of these spatial differences, we identified the pri-  
448 mary meteorological drivers of GPP and NEP based on the standardized regression coefficients  
449 (Fig. 5c, d, and Table 2). The results indicate that for GPP, diffuse radiation accounts for the  
450 largest proportion (77.83%), followed by vapor pressure deficit (9.27%) and direct radiation  
451 (8.4%), while the influence of temperature (4.45%) and precipitation (0.05%) is relatively  
452 small. For NEP, diffuse radiation remains the dominant driver (72.2%), followed by direct  
453 radiation (15.92%) and temperature (5.64%). These results highlight that aerosols modify the  
454 radiation composition, particularly by enhancing diffuse radiation, which substantially in-  
455 creases photosynthetic efficiency and strengthens the regional carbon sink. In contrast, the ef-  
456 fects of temperature and VPD are weaker overall but more pronounced in northern arid and  
457 semi-arid regions, where water limitation constrains carbon uptake. Collectively, these findings  
458 confirm that radiation composition primarily controls the spatiotemporal dynamics of China's  
459 terrestrial carbon sink, while temperature and moisture factors exert region-dependent modu-  
460 lations.

461

462 **Table 2.** Proportion of dominant meteorological factors for GPP and NEP across China  
463 (Units: %).

Factors	RadD (%)	RadF (%)	Temp (%)	Precip (%)	VPD(%)
GPP	8.4	77.83	4.45	0.05	9.27
NEP	15.92	72.2	5.64	0.14	6.1

464

465

466

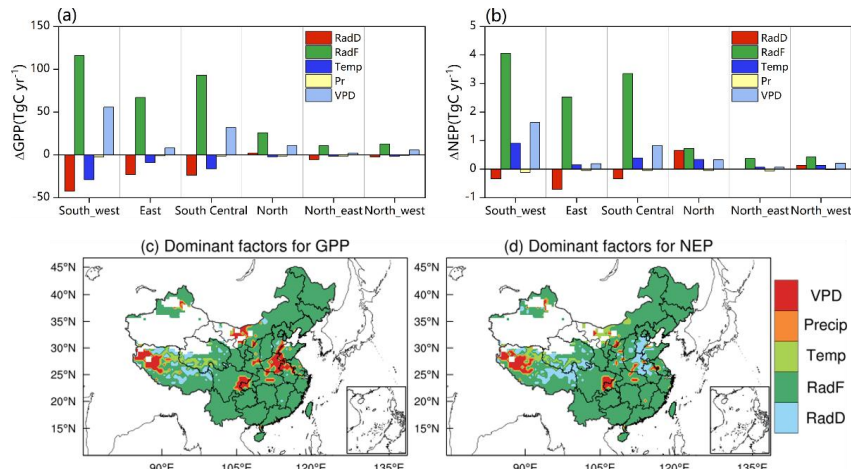
467

468



469

470



471

472 **Figure 5.** Effect of aerosol-induced changes in meteorological factors on GPP and NEP, and  
473 spatial patterns of dominant factors. (a) Regional contributions of individual meteorological  
474 factors to GPP; (b) Regional contributions of individual meteorological factors to NEP; (c)  
475 Spatial distribution of the dominant meteorological factor for GPP; (d) Spatial distribution of  
476 the dominant meteorological factor for NEP.

477

### 478 3.3 Effects of surface ozone on carbon sinks

479 During 2010–2020, surface  $O_3$  in China increased and imposed a persistent suppression  
480 on terrestrial carbon sinks. Simulations show a strong reduction of GPP by  $0.4\text{--}0.6 \text{ gC m}^{-2} \text{ day}^{-1}$   
481 in most regions, with more than  $0.8 \text{ gC m}^{-2} \text{ day}^{-1}$  in Southeast and Southwest China (Fig. 6a).  
482 NEP shows a similar spatial pattern (Fig. 6b). The largest decline occurs in the southeast (Yang-  
483 tze River basin and South China coast), with NEP reduced by  $0.06\text{--}0.08 \text{ gC m}^{-2} \text{ day}^{-1}$  and  
484 locally above  $0.1 \text{ gC m}^{-2} \text{ day}^{-1}$ , consistent with high  $O_3$  and evergreen broadleaf forests (Yue et  
485 al., 2017). In the southwest (Sichuan Basin and Yunnan–Guizhou Plateau), NEP decreases by  
486  $0.03\text{--}0.06 \text{ gC m}^{-2} \text{ day}^{-1}$ , related to complex terrain and dense forests. Impacts are weaker in  
487 Northeast and Northwest China, mostly below  $0.02 \text{ gC m}^{-2} \text{ day}^{-1}$ . In Shandong, Henan, and  
488 northern Jiangsu, the simulated losses are small, reflecting cropland-dominated land cover.

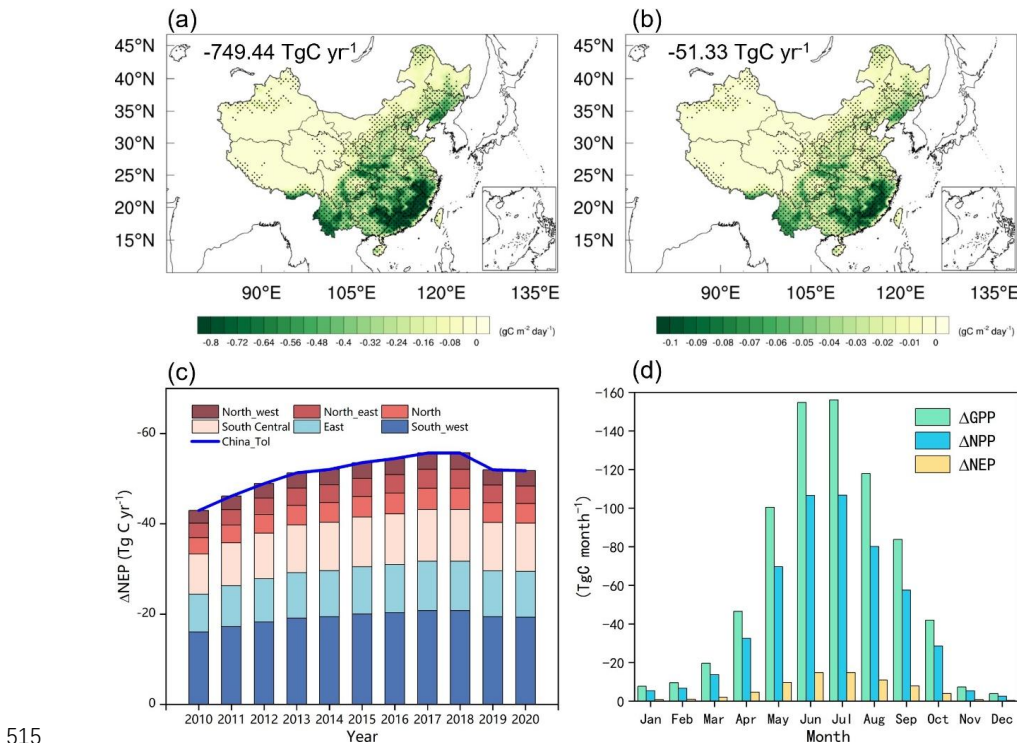


489 However, earlier studies reported strong O<sub>3</sub> effects on crops (Ren et al., 2012), suggesting pos-  
490 sible underestimation. This bias may stem from the simplified crop representation in the model  
491 (Fig. S2). Nationwide, O<sub>3</sub> reduces GPP and NEP by 749.44 TgC yr<sup>-1</sup> and 51.33 TgC yr<sup>-1</sup>, ac-  
492 counting for 10.17 % and 12.9 % of the totals. The suppression is attributed to reduced photo-  
493 synthesis, altered stomatal conductance, and shifts in carbon allocation, which together weaken  
494 ecosystem sinks.

495 The annual effect intensifies until 2018 and then weakens (Fig. 6c). In 2010, O<sub>3</sub> reduces  
496 NEP by 42.93 TgC yr<sup>-1</sup>, reaching 55.71 TgC yr<sup>-1</sup> in 2018. It then decreases to 51.98 TgC yr<sup>-1</sup>  
497 in 2019 and 51.77 TgC yr<sup>-1</sup> in 2020. These variations reflect air pollution control policies. Be-  
498 tween 2013 and 2017, the first Clean Air Action reduced PM<sub>2.5</sub> and NOx but left volatile or-  
499 ganic compounds (VOCs) largely uncontrolled, thereby enhancing O<sub>3</sub> formation, especially in  
500 VOCs-limited regions (Lu et al., 2020). Both model and observations show higher O<sub>3</sub> during  
501 this stage (Fig. S4). After 2018, the second Clean Air Action introduced coordinated control of  
502 NOx and VOCs in the Yangtze River Delta and Pearl River Delta, reducing O<sub>3</sub> during summer  
503 and easing sink suppression in 2019–2020. In contrast, O<sub>3</sub> continued to rise in North China,  
504 indicating uneven policy outcomes across regions.

505 Seasonal effects are distinct (Fig. 6d and Fig. S9). Summer shows the strongest suppres-  
506 sion, with NEP reduced by 29.1 TgC (56.69 % of the annual effect). This results from the  
507 overlap of peak O<sub>3</sub> and peak photosynthesis, when high temperature and humidity keep stomata  
508 open and allow O<sub>3</sub> uptake. Spring is second, with NEP reduced by 11.67 TgC (22.74 %). The  
509 effect is linked to leaf expansion, rapid growth, and frequent transport events. Autumn and  
510 winter show weaker impacts due to lower photosynthesis, unfavorable O<sub>3</sub> chemistry, and re-  
511 duced stomatal conductance. Regional differences are evident: in the south, suppression ex-  
512 tends from spring to late autumn, while in the north it is confined to summer. This highlights  
513 the role of climate and phenology in modulating the impact of O<sub>3</sub> on carbon sinks.

514



515 **Figure 6.** Spatiotemporal variations in O<sub>3</sub>-induced changes in carbon fluxes during 2010–2020.

516 **Figure 6.** Spatiotemporal variations in O<sub>3</sub>-induced changes in carbon fluxes during 2010–2020.  
 517 (a–b) Multi-year mean spatial patterns of O<sub>3</sub>-induced changes in GPP and NEP. National totals  
 518 are shown in each panel. Black dots denote significant changes ( $p < 0.01$ ). (c) Interannual  
 519 variation of O<sub>3</sub>-induced NEP. (d) O<sub>3</sub>-induced monthly variations in GPP, NPP, and NEP.

520

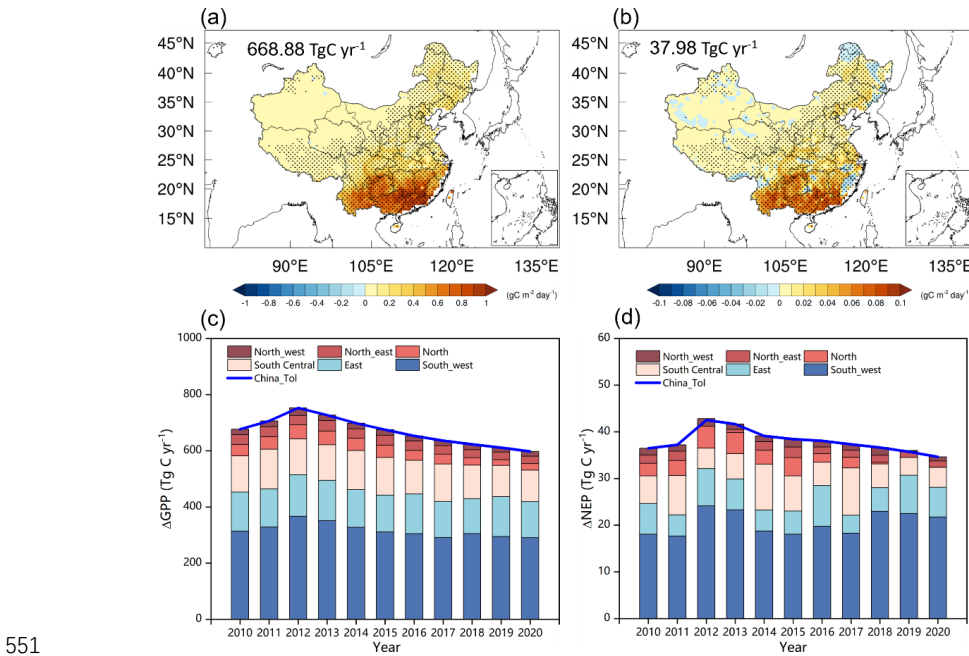
### 521 **3.4 Effects of atmospheric nitrogen deposition on carbon sinks**

522 The response of China's terrestrial ecosystems to atmospheric nitrogen deposition during  
 523 2010–2020 shows pronounced spatial heterogeneity (Fig. 7a, b). At the national scale, nitrogen  
 524 deposition increased GPP and NEP by 668.88 TgC yr<sup>-1</sup> and 37.98 TgC yr<sup>-1</sup>, respectively. These  
 525 increases account for 9.08% of total GPP and 9.52% of total NEP. The net gains were mainly  
 526 concentrated in the southeastern, southwestern, and central regions. In these areas, NEP in-  
 527 creased by 0.04–0.08 g C m<sup>-2</sup> day<sup>-1</sup>, forming the dominant contribution to the nitrogen-induced  
 528 carbon sink. Although atmospheric nitrogen deposition is highest in eastern China (Fig. 2e, f),  
 529 the regional variations in GPP and NEP induced by nitrogen deposition are more pronounced



530 in southern China than in the east. The strong spatial gradient highlights that the ecological  
531 effects of nitrogen deposition are not uniform, but tightly linked to anthropogenic nitrogen  
532 emissions and ecosystem sensitivity (Shang et al., 2024). High responses were observed in  
533 regions with intensive agriculture and industry, where deposition exceeded  $15 \text{ kg N ha}^{-1} \text{ yr}^{-1}$ .  
534 Vegetation dominated by subtropical evergreen broadleaf forests, mixed forests, and croplands  
535 is generally nitrogen-limited. Additional nitrogen input alleviated nutrient constraints, en-  
536 hanced photosynthesis and biomass accumulation, and shifted soil microbial processes. When  
537 stimulation of GPP and NPP outweighed the increase in ER, NEP rose. Warm and humid cli-  
538 mates, together with long growing seasons, further amplified these effects.

539 The impacts of nitrogen deposition on GPP and NEP varied strongly over time (Fig. 7c,  
540 d). In 2010, deposition enhanced NEP by  $36.45 \text{ TgC yr}^{-1}$ . The effect increased to a peak of  $42.5$   
541  $\text{TgC yr}^{-1}$  in 2012, but then declined, reaching  $34.65 \text{ TgC yr}^{-1}$  by 2020. This trajectory reflects  
542 the influence of China's air pollution control policies on ecosystem carbon dynamics. The tem-  
543 poral trend corresponds to changes in nitrogen deposition fluxes. Between 2010 and 2012, rapid  
544 industrialization and agriculture raised deposition from  $15.85$  to  $17.91 \text{ kg N ha}^{-1} \text{ yr}^{-1}$  (+13%).  
545 After 2013, emission reduction policies reduced nitrogen deposition, which fell to  $13.25 \text{ kg N}$   
546  $\text{ha}^{-1} \text{ yr}^{-1}$  in 2020 (-26.02%). Notably, the effect of nitrogen deposition on NEP leveled off after  
547 2015, which can be attributed to the slower decline rate of atmospheric nitrogen deposition  
548 since 2015 (Fig. S5). The reduction in NEP (-18.47%) was smaller than that in nitrogen input.  
549 This lagged response suggests that soil nitrogen pools accumulated from long-term deposition  
550 continued to supply nitrogen to vegetation, buffering the decline.



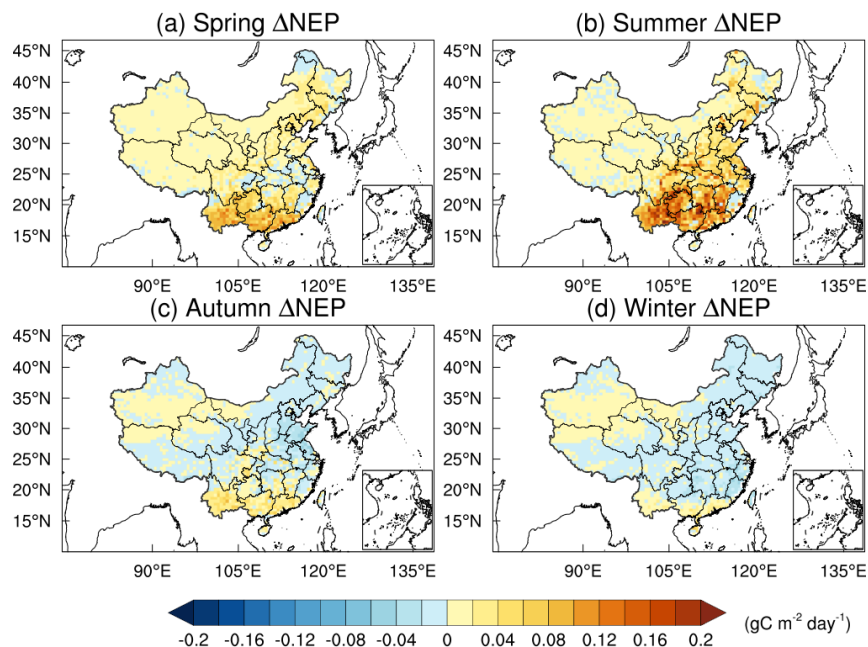
551  
552 **Figure 7.** Spatiotemporal variations in Ndep-induced changes in carbon fluxes during 2010–  
553 2020. (a–b) Multi-year mean spatial patterns of Ndep-induced changes in GPP and NEP. Na-  
554 tional totals are shown in each panel. Black dots denote significant changes ( $p < 0.01$ ). (c–d)  
555 Interannual variation of Ndep-induced in GPP and NEP.

556

557 The influence of nitrogen deposition on NEP displayed clear seasonality (Fig. 8). Strong  
558 positive effects occurred in summer and spring, while autumn and winter showed suppression.  
559 Summer accounted for the largest gain, with an NEP increase of 27.16 TgC. Spring followed  
560 with 14.12 TgC. In contrast, autumn and winter reduced NEP by 0.2 and 3.1 TgC, respectively.  
561 These seasonal differences result from the combined influence of multiple factors. During sum-  
562 mer, optimal temperature, light, and water supported vigorous canopy photosynthesis. Plants  
563 assimilated nitrogen efficiently, leading to higher GPP and biomass accumulation. Spring  
564 growth stages were also nitrogen-sensitive, producing strong positive responses. In autumn and  
565 winter, however, plant activity slowed. Nitrogen inputs mainly stimulated heterotrophic respi-  
566 ration, while GPP and NPP remained low. As a result, NEP decreased, and carbon sink strength  
567 weakened outside the growing season.



568



569

570 **Figure 8.** Spatial distribution of Ndep-induced seasonal variations in NEP during 2010–2020  
571 (units:  $\text{gC m}^{-2} \text{ day}^{-1}$ ). (a) Spring, including March, April, and May. (b) Summer, including June,  
572 July, and August. (c) Autumn, including September, October, and November. (d) Winter, in-  
573 cluding January, February, and December.

574

### 575 **3.5 Integrated Impact Analysis**

576 To assess the combined influence of aerosols,  $\text{O}_3$ , and atmospheric nitrogen deposition on  
577 China's terrestrial carbon sink, the three independent effects were algebraically summed. Dur-  
578 ing 2010–2020, the co-evolution of these atmospheric factors jointly drove substantial interan-  
579 nual variability and stage-dependent changes in carbon uptake, closely linked to the implemen-  
580 tation of the CAA plan. The interannual trend (Fig. 9) shows that although aerosols and nitrogen  
581 deposition generally enhanced carbon sequestration, the strong carbon loss caused by  $\text{O}_3$   
582 largely offset these positive effects. The mean net effect was  $4.58 \text{ TgC yr}^{-1}$ , exhibiting pro-  
583 nounced fluctuations and a declining trend. Net enhancement was strong in the early years of  
584 the decade but weakened steadily and approached neutral levels by 2018–2020, when a slight



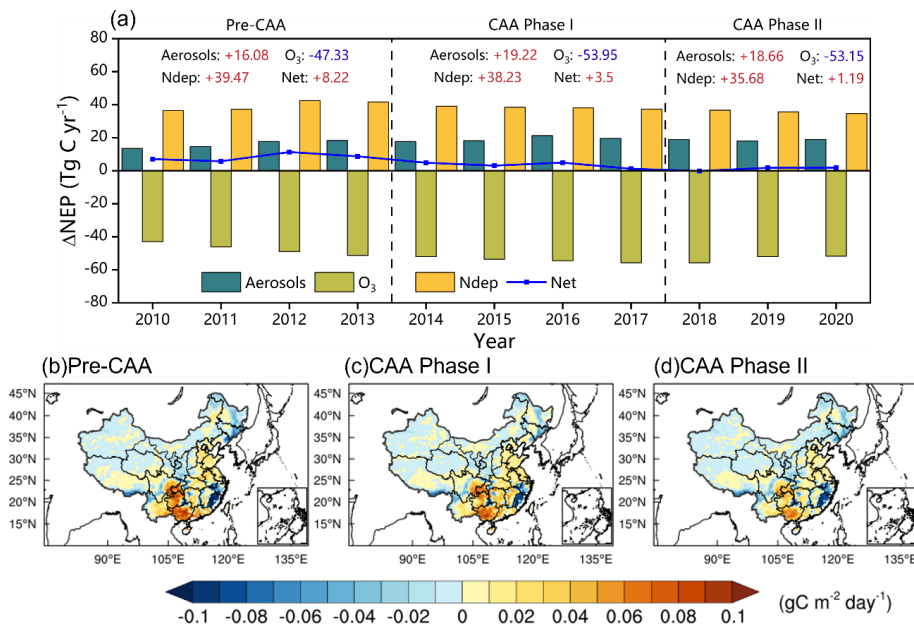
585 negative value (-0.14 TgC yr<sup>-1</sup>) first appeared. These changes indicate a gradual transition from  
586 an enhancement-dominated to an inhibition-dominated regime.

587 To further interpret this transition, the study period was divided into three phases accord-  
588 ing to key CAA milestones, and the dominant factors were identified (Fig. 9a). In pre-CAA  
589 (2010–2013), the mean annual net effect reached 8.22 TgC yr<sup>-1</sup>, characterized by nitrogen-  
590 deposition-dominated enhancement. Nitrogen deposition provided the largest positive contri-  
591 bution (+39.47 TgC yr<sup>-1</sup>), while the diffuse-radiation fertilization effect of aerosols offered a  
592 secondary gain (+16.08 TgC yr<sup>-1</sup>). The negative impact of O<sub>3</sub> (-47.33 TgC yr<sup>-1</sup>) was largely  
593 compensated by the two positive drivers, resulting in a pronounced increase in carbon sink  
594 strength. During CAA Phase I (2014–2017), the mean net effect decreased sharply to 3.50 TgC  
595 yr<sup>-1</sup>, marking a transitional stage with competing influences. The positive effect of aerosols  
596 peaked (+19.22 TgC yr<sup>-1</sup>), likely due to enhanced scattering as absorbing components were  
597 preferentially reduced. However, this gain was largely offset by intensified O<sub>3</sub>-induced inhibi-  
598 tion (-53.80 TgC yr<sup>-1</sup>). In CAA Phase II (2018–2020), the mean net effect further declined to  
599 1.19 TgC yr<sup>-1</sup>, forming an O<sub>3</sub>-dominated pattern. With continued emission control, the aerosol-  
600 induced enhancement decreased from its peak (+18.66 TgC yr<sup>-1</sup>), and the nitrogen-deposition  
601 gain weakened (+35.68 TgC yr<sup>-1</sup>). Although O<sub>3</sub> suppression slightly eased (-53.15 TgC yr<sup>-1</sup>), it  
602 still nearly balanced the combined positive contributions, indicating a fundamental shift in at-  
603 mospheric drivers controlling China's terrestrial carbon sink.

604 The spatial overlay further supports these findings (Fig. 9b, c, d). In forested and indus-  
605 trialized regions of eastern and southern China, the cancellation between positive and negative  
606 effects was most pronounced. These areas, benefiting from nitrogen and aerosol fertilization  
607 but suffering from intense O<sub>3</sub> pollution, became hotspots of weakened or even reversed net  
608 effects. Overall, the CAA plan not only improved air quality but also altered atmospheric com-  
609 position in ways that substantially affected China's terrestrial carbon sinks. Policy-driven emis-  
610 sion changes transformed the system from a nitrogen–aerosol-enhanced regime to an O<sub>3</sub>-dom-  
611 inated offset pattern. These results suggest that achieving synergistic benefits between air-qual-  
612 ity improvement and carbon neutrality requires elevating O<sub>3</sub> mitigation to a higher strategic  
613 priority.



614



615

616 **Figure 9.** The overall impacts of aerosols, O<sub>3</sub>, and atmospheric nitrogen deposition on the  
617 terrestrial carbon sink in China during 2010–2020. (a) Interannual variations of the combined  
618 effects. Pre-CAA represents the period before the implementation of the Clean Air Action  
619 (2010–2013); CAA Phase I and CAA Phase II represent the first (2014–2017) and second  
620 (2018–2020) stages of the CAA, respectively. (b–d) Spatial distributions of the annual means  
621 during the Pre-CAA, CAA Phase I, and CAA Phase II periods.

622

### 623 3.6 Uncertainties

624 Although the RegESM framework captures the overall spatiotemporal variations of  
625 China's terrestrial carbon sink in response to atmospheric composition changes, several uncer-  
626 tainties remain that may influence the quantitative assessment of the individual and combined  
627 effects of aerosols, O<sub>3</sub>, and nitrogen deposition.

628 First, this study only considered the direct radiative effects of aerosols, while aerosol–  
629 cloud interactions were excluded. The first and second indirect effects of aerosols on cloud  
630 formation and albedo involve large uncertainties (Haywood and Boucher, 2000) and were



631 therefore not represented in our simulations. However, observations have shown that terrestrial  
632 carbon fluxes are highly sensitive to sky conditions and diffuse radiation changes (Oliphant et  
633 al., 2011; Yue and Unger, 2017). The omission of aerosol–cloud interactions may affect the  
634 magnitude and spatial pattern of aerosol impacts on radiation and photosynthesis, as cloud-  
635 mediated diffuse radiation responses remain uncertain. Future work should explicitly include  
636 aerosol–cloud–radiation feedbacks to better quantify their effects on ecosystem carbon ex-  
637 change.

638 Second, uncertainties remain in evaluating vegetation responses to O<sub>3</sub> exposure. Field-  
639 based O<sub>3</sub> fumigation experiments across China are still limited, making it difficult to compre-  
640 hensively assess ecosystem-level damage. In this study, the YIBs model applied different O<sub>3</sub>  
641 damage coefficients for plant functional types, and the parameterization has shown reasonable  
642 regional performance in simulating GPP–O<sub>3</sub> responses (Yue et al., 2017). Nevertheless, a wider  
643 range of site-level observations is required to constrain the O<sub>3</sub> damage functions across various  
644 vegetation types and climate zones at the national scale.

645 Third, nonlinear coupling among aerosols, O<sub>3</sub>, and nitrogen deposition introduces sys-  
646 temic uncertainty in estimating their combined effects. Aerosol reduction alters photolysis rates  
647 and thereby affects O<sub>3</sub> formation (Tang et al., 2017; Yan et al., 2023; Yang et al., 2022), while  
648 O<sub>3</sub> and nitrogen jointly regulate stomatal conductance, photosynthetic efficiency, and water-  
649 use dynamics (Sitch et al., 2007; Zhang et al., 2018). These interactions may amplify or offset  
650 each other under changing climatic conditions, emphasizing the need for high-resolution, fully  
651 coupled chemistry–ecosystem modeling frameworks to capture the co-evolution of multiple  
652 atmospheric processes.

653 In summary, despite these uncertainties, this study provides robust quantitative evidence  
654 that aerosols, O<sub>3</sub>, and nitrogen deposition jointly modified the magnitude and spatial distribu-  
655 tion of China’s terrestrial carbon sink during 2010–2020. Future efforts should focus on incor-  
656 porating aerosol–cloud interactions, expanding field-based O<sub>3</sub> response networks, and improv-  
657 ing representation of multi-process coupling to further constrain atmospheric–biosphere feed-  
658 backs under China’s evolving air quality and carbon neutrality goals.

659



660 **4 Conclusions**

661 This study employed the RegESM to quantify the effects of aerosol, surface O<sub>3</sub>, and ni-  
662 trogen deposition on China's terrestrial carbon sink during 2010–2020. The model effectively  
663 reproduced the spatial and temporal variations of aerosol optical depth, O<sub>3</sub>, nitrogen deposition,  
664 and carbon fluxes, providing a solid basis for process-level attribution analysis.

665 Aerosols exerted a substantial positive influence on China's terrestrial carbon sink. On  
666 average, aerosols enhanced GPP and NEP by 293.28 TgC yr<sup>-1</sup> (3.98%) and 17.93 TgC yr<sup>-1</sup>  
667 (4.49%), respectively, primarily through the diffuse radiation fertilization effect. The strongest  
668 enhancement appeared in southern and eastern China, where high aerosol loading and dense  
669 vegetation synergistically improved canopy light-use efficiency. Aerosol-induced surface cool-  
670 ing and reduced VPD further alleviated water stress and stimulated carbon uptake. The en-  
671 hancement peaked during 2015–2017, coinciding with elevated diffuse radiation fractions, and  
672 weakened slightly under cleaner atmospheric conditions after 2018.

673 In contrast, surface O<sub>3</sub> persistently suppressed ecosystem carbon uptake, reducing GPP  
674 and NEP by 749.44 TgC yr<sup>-1</sup> (10.17%) and 51.33 TgC yr<sup>-1</sup> (12.9%), respectively. The strongest  
675 suppression occurred in southeastern and southwestern China, where dense forest ecosystems  
676 coincided with high O<sub>3</sub> concentrations. O<sub>3</sub>-induced damage peaked in 2018, consistent with the  
677 exceptionally high O<sub>3</sub> levels. Subsequent coordinated NO<sub>x</sub>–VOCs management under the sec-  
678 ond Clean Air Action partially mitigated O<sub>3</sub> levels and NEP suppression. O<sub>3</sub> exerted a strongly  
679 seasonal negative impact on NEP, with the strongest suppression occurring in summer.

680 Atmospheric nitrogen deposition enhanced the terrestrial carbon sink by 9.08% for GPP  
681 and 9.52% for NEP, with effects concentrated in southern and central China. The enhancement  
682 peaked around 2012, declined gradually after 2013 following reduced anthropogenic emissions,  
683 and leveled off after 2015, corresponding to a slower decline in deposition and a lagged eco-  
684 system response due to soil nitrogen accumulation. Seasonal variations showed stronger stim-  
685 ulation in summer and spring, while autumn and winter exhibited minor reductions linked to  
686 enhanced respiration.

687 During 2010–2020, the combined effects of aerosols, surface O<sub>3</sub>, and atmospheric nitro-  
688 gen deposition on China's terrestrial carbon sink exhibited marked interannual variability and



689 a distinct transition under the Clean Air Action (CAA). The net atmospheric contribution de-  
690 clined from  $+8.22 \text{ Tg C yr}^{-1}$  during the Pre-CAA period (2010–2013) to  $+1.19 \text{ Tg C yr}^{-1}$  in  
691 Phase II (2018–2020), as the increasing suppression from  $\text{O}_3$  ( $-53.15 \text{ Tg C yr}^{-1}$ ) gradually offset  
692 the positive impacts of aerosols and nitrogen deposition. These results indicate that China's air-  
693 pollution control not only improved air quality but also altered atmospheric chemical compo-  
694 sition in ways that significantly affected ecosystem carbon uptake, with  $\text{O}_3$  becoming the dom-  
695 inant limiting factor in the later period.

696 Overall, aerosols,  $\text{O}_3$ , and nitrogen deposition exerted interconnected yet contrasting in-  
697 fluences on China's terrestrial carbon sink. Aerosols and nitrogen deposition enhanced carbon  
698 uptake through diffuse radiation and nutrient input, whereas  $\text{O}_3$  caused physiological damage  
699 that suppressed it. The evolving interplay among these factors illustrates how emission reduc-  
700 tions, atmospheric chemistry, and ecosystem feedbacks jointly impact carbon sink dynamics  
701 under China's clean-air policies. Strengthening integrated  $\text{O}_3$  control is therefore essential to  
702 secure co-benefits for air quality improvement and carbon neutrality goals.

### 703 **Data Availability Statement**

704 MODIS data are provided at <https://doi.org/10.5067/MODIS/MOD17A2H.006> (last access: 11  
705 May 2024; Running et al., 2015). AOD data come from the MODIS Level-3 monthly product  
706 (MOD08\_M3, Collection 6.1) available at [https://doi.org/10.5067/MODIS/MOD08\\_M3.061](https://doi.org/10.5067/MODIS/MOD08_M3.061)  
707 (last access: 5 November 2024; Platnick et al., 2015). WDCGG data are available at  
708 <https://doi.org/10.15138/wkgj-f215> (last access: 10 June 2024; Lan, 2023). ERA-Interim data  
709 are available at <https://doi.org/10.24381/cds.f2f5241d> (last access: 8 June 2024; Dee et al.,  
710 2011). The Carbon Tracker data can be accessed at <https://gml.noaa.gov/ccgg/carbontracker/>  
711 (last access: 21 June 2024; Jacobson et al., 2023). CNEMC data are provided at  
712 <https://www.cnemc.cn/en> (Kong et al., 2021).

### 713 **Author contributions**

714 TW and NX designed the study. NX performed the analysis, conducted the evaluation, and  
715 drafted the manuscript. TW supervised the research and acquired funding. Both authors con-  
716 tributed to the interpretation of results and to reviewing and editing the manuscript.



717 **Competing interests**

718 The corresponding author has stated that all the authors have no conflicts of interest.

719 **Disclaimer**

720 Publisher's note: Copernicus Publications remains neutral with regard to jurisdictional claims  
721 made in the text, published maps, institutional affiliations, or any other geographical representation  
722 in this paper. The authors bear the ultimate responsibility for providing appropriate place  
723 names. Views expressed in the text are those of the authors and do not necessarily reflect the  
724 views of the publisher.

725 **Acknowledgments**

726 We would like to acknowledge the anthropogenic emission inventory support from Tsinghua  
727 University and the observed data from the China National Environmental Monitoring Center.  
728 We also gratefully acknowledge a wide range of other institutional partners.

729 **Financial support**

730 This work was supported by the National Key Basic Research Development Program of China  
731 (2024YFC3711905) and the National Natural Science Foundation of China (42477103).

732 **References**

733 Cao, S., He, Y., Zhang, L., Sun, Q., Zhang, Y., Li, H., Wei, X., and Liu, Y.: Spatiotemporal  
734 dynamics of vegetation net ecosystem productivity and its response to drought in  
735 Northwest China, *GIScience & Remote Sensing*, 60, 2194597,  
736 <https://doi.org/10.1080/15481603.2023.2194597>, 2023.

737 Cen, X., He, N., Van Sundert, K., Yu, K., Li, M., Xu, L., He, L., and Butterbach-Bahl, K.:  
738 Global patterns of nitrogen saturation in forests, *One Earth*, 8,  
739 <https://doi.org/10.1016/j.oneear.2024.10.007>, 2025.

740 Chen, H., Li, D., Gurmesa, G. A., Yu, G., Li, L., Zhang, W., Fang, H., and Mo, J.: Effects of  
741 nitrogen deposition on carbon cycle in terrestrial ecosystems of China: A meta-analysis,



742 Environ. Pollut., 206, 352-360, <https://doi.org/10.1016/j.envpol.2015.07.033>, 2015.

743 Dee, D. P., Uppala, S. M., Simmons, A. J., Berrisford, P., Poli, P., Kobayashi, S., Andrae, U.,  
744 Balmaseda, M. A., Balsamo, G., Bauer, P., Bechtold, P., Beljaars, A. C. M., van de Berg,  
745 L., Bidlot, J., Bormann, N., Delsol, C., Dragani, R., Fuentes, M., Geer, A. J., Haimberger,  
746 L., Healy, S. B., Hersbach, H., Hólm, E. V., Isaksen, L., Källberg, P., Köhler, M.,  
747 Matricardi, M., McNally, A. P., Monge-Sanz, B. M., Morcrette, J. J., Park, B. K., Peubey,  
748 C., de Rosnay, P., Tavolato, C., Thépaut, J. N., and Vitart, F.: The ERA-Interim reanalysis:  
749 configuration and performance of the data assimilation system, QJRMS, 137, 553-597,  
750 <https://doi.org/10.1002/qj.828>, 2011.

751 Doughty, C. E., Flanner, M. G., and Goulden, M. L.: Effect of smoke on subcanopy shaded  
752 light, canopy temperature, and carbon dioxide uptake in an Amazon rainforest, Global  
753 Biogeochemical Cycles, 24, <https://doi.org/10.1029/2009gb003670>, 2010.

754 Emmons, L. K., Walters, S., Hess, P. G., Lamarque, J. F., Pfister, G. G., Fillmore, D., Granier,  
755 C., Guenther, A., Kinnison, D., Laepple, T., Orlando, J., Tie, X., Tyndall, G., Wiedinmyer,  
756 C., Baugcum, S. L., and Kloster, S.: Description and evaluation of the Model for Ozone  
757 and Related chemical Tracers, version 4 (MOZART-4), Geosci. Model Dev., 3, 43-67,  
758 <https://doi.org/10.5194/gmd-3-43-2010>, 2010.

759 Feng, Z., Hu, E., Wang, X., Jiang, L., and Liu, X.: Ground-level O<sub>3</sub> pollution and its impacts  
760 on food crops in China: A review, Environ. Pollut., 199, 42-48,  
761 <https://doi.org/10.1016/j.envpol.2015.01.016>, 2015.

762 Friedlingstein, P., O'Sullivan, M., Jones, M. W., Andrew, R. M., Bakker, D. C. E., Hauck, J.,  
763 Landschützer, P., Le Quéré, C., Luijkx, I. T., Peters, G. P., Peters, W., Pongratz, J.,  
764 Schwingshackl, C., Sitch, S., Canadell, J. G., Ciais, P., Jackson, R. B., Alin, S. R., Anthoni,  
765 P., Barbero, L., Bates, N. R., Becker, M., Bellouin, N., Decharme, B., Bopp, L., Brasika,  
766 I. B. M., Cadule, P., Chamberlain, M. A., Chandra, N., Chau, T.-T.-T., Chevallier, F., Chini,  
767 L. P., Cronin, M., Dou, X., Enyo, K., Evans, W., Falk, S., Feely, R. A., Feng, L., Ford, D.  
768 J., Gasser, T., Ghattas, J., Gkritzalis, T., Grassi, G., Gregor, L., Gruber, N., Gürses, Ö.,  
769 Harris, I., Hefner, M., Heinke, J., Houghton, R. A., Hurt, G. C., Iida, Y., Ilyina, T.,  
770 Jacobson, A. R., Jain, A., Jarníková, T., Jersild, A., Jiang, F., Jin, Z., Joos, F., Kato, E.,



771 Keeling, R. F., Kennedy, D., Klein Goldewijk, K., Knauer, J., Korsbakken, J. I., Körtzinger,  
772 A., Lan, X., Lefèvre, N., Li, H., Liu, J., Liu, Z., Ma, L., Marland, G., Mayot, N., McGuire,  
773 P. C., McKinley, G. A., Meyer, G., Morgan, E. J., Munro, D. R., Nakaoka, S.-I., Niwa, Y.,  
774 O'Brien, K. M., Olsen, A., Omar, A. M., Ono, T., Paulsen, M., Pierrot, D., Pocock, K.,  
775 Poulter, B., Powis, C. M., Rehder, G., Resplandy, L., Robertson, E., Rödenbeck, C., Rosan,  
776 T. M., Schwinger, J., Séferian, R., Smallman, T. L., Smith, S. M., Sospedra-Alfonso, R.,  
777 Sun, Q., Sutton, A. J., Sweeney, C., Takao, S., Tans, P. P., Tian, H., Tilbrook, B., Tsujino,  
778 H., Tubiello, F., van der Werf, G. R., van Ooijen, E., Wanninkhof, R., Watanabe, M.,  
779 Wimart-Rousseau, C., Yang, D., Yang, X., Yuan, W., Yue, X., Zaehle, S., Zeng, J., and  
780 Zheng, B.: Global Carbon Budget 2023, *Earth System Science Data*, 15, 5301-5369,  
781 https://doi.org/10.5194/essd-15-5301-2023, 2023.

782 Geng, G. N., Liu, Y. X., Liu, Y., Liu, S. G., Cheng, J., Yan, L., Wu, N. N., Hu, H. W., Tong, D.,  
783 Zheng, B., Yin, Z. C., He, K. B., and Zhang, Q.: Efficacy of China's clean air actions to  
784 tackle PM<sub>2.5</sub> pollution between 2013 and 2020, *Nature Geoscience*, 17,  
785 https://doi.org/10.1038/s41561-024-01540-z, 2024.

786 Giorgi, F., Coppola, E., Solmon, F., Mariotti, L., Sylla, M. B., Bi, X., Elguindi, N., Diro, G. T.,  
787 Nair, V., Giuliani, G., Turuncoglu, U. U., Cozzini, S., Guttler, I., O'Brien, T. A., Tawfik,  
788 A. B., Shalaby, A., Zakey, A. S., Steiner, A. L., Stordal, F., Sloan, L. C., and Brankovic,  
789 C.: RegCM4: model description and preliminary tests over multiple CORDEX domains,  
790 *Clim. Res.*, 52, 7-29, https://doi.org/10.3354/cr01018, 2012.

791 Gu, L. H., Baldocchi, D. D., Wofsy, S. C., Munger, J. W., Michalsky, J. J., Urbanski, S. P., and  
792 Boden, T. A.: Response of a deciduous forest to the Mount Pinatubo eruption: Enhanced  
793 photosynthesis, *Science*, 299, 2035-2038, https://doi.org/10.1126/science.1078366, 2003.

794 Hao, Y., Meng, X., Yu, X., Lei, M., Li, W., Yang, W., Shi, F., and Xie, S.: Quantification of  
795 primary and secondary sources to PM<sub>2.5</sub> using an improved source regional apportionment  
796 method in an industrial city, China, *Sci. Total Environ.*, 706,  
797 https://doi.org/10.1016/j.scitotenv.2019.135715, 2020.

798 Haywood, J. and Boucher, O.: Estimates of the direct and indirect radiative forcing due to  
799 tropospheric aerosols: A review, *Reviews of Geophysics*, 38, 513-543,



800        <https://doi.org/10.1029/1999rg000078>, 2000.

801        He, M. Z., Kimball, J. S., Maneta, M. P., Maxwell, B. D., Moreno, A., Begueria, S., and Wu, X. C.: Regional Crop Gross Primary Productivity and Yield Estimation Using Fused Landsat-MODIS Data, *Remote Sens.*, 10, 372, <https://doi.org/10.3390/rs10030372>, 2018.

804        Hersbach, H., Bell, B., Berrisford, P., Hirahara, S., Horányi, A., Muñoz-Sabater, J., Nicolas, J., Peubey, C., Radu, R., Schepers, D., Simmons, A., Soci, C., Abdalla, S., Abellan, X., Balsamo, G., Bechtold, P., Biavati, G., Bidlot, J., Bonavita, M., De Chiara, G., Dahlgren, P., Dee, D., Diamantakis, M., Dragani, R., Flemming, J., Forbes, R., Fuentes, M., Geer, A., Haimberger, L., Healy, S., Hogan, R. J., Hólm, E., Janisková, M., Keeley, S., Laloyaux, P., Lopez, P., Lupu, C., Radnoti, G., de Rosnay, P., Rozum, I., Vamborg, F., Villaume, S., and Thépaut, J. N.: The ERA5 global reanalysis, *QJRMS*, 146, 1999-2049, <https://doi.org/10.1002/qj.3803>, 2020.

812        Horowitz, L. W., Walters, S., Mauzerall, D. L., Emmons, L. K., Rasch, P. J., Granier, C., Tie, X. X., Lamarque, J. F., Schultz, M. G., Tyndall, G. S., Orlando, J. J., and Brasseur, G. P.: A global simulation of tropospheric ozone and related tracers: Description and evaluation of MOZART, version 2, *J. Geophys. Res.: Atmos.*, 108, 4784, <https://doi.org/10.1029/2002jd002853>, 2003.

817        Jacobson, A. R., Schuldt, K. N., Tans, P., Arlyn Andrews, Miller, J. B., Oda, T., Mund, J., Weir, B., Ott, L., Aalto, T., Abshire, J. B., Aikin, K., Aoki, S., Apadula, F., Arnold, S., Baier, B., Bartyzel, J., Beyersdorf, A., Biermann, T., ... Miroslaw Zimnoch.: CarbonTracker CT2022, NOAA Global Monitoring Laboratory, [data set], <https://doi.org/10.25925/Z1GJ-3254>, 2023.

822        Jung, M., Reichstein, M., Schwalm, C. R., Huntingford, C., Sitch, S., Ahlstrom, A., Arneth, A., Camps-Valls, G., Ciais, P., Friedlingstein, P., Gans, F., Ichii, K., Ain, A. K. J., Kato, E., Papale, D., Poulter, B., Raduly, B., Rodenbeck, C., Tramontana, G., Viovy, N., Wang, Y.-P., Weber, U., Zaehle, S., and Zeng, N.: Compensatory water effects link yearly global land CO<sub>2</sub> sink changes to temperature, *Nature*, 541, 516-520, <https://doi.org/10.1038/nature20780>, 2017.

828        Kong, L., Tang, X., Zhu, J., Wang, Z. F., Li, J. J., Wu, H. J., Wu, Q. Z., Chen, H. S., Zhu, L. L.,



829 Wang, W., Liu, B., Wang, Q., Chen, D. H., Pan, Y. P., Song, T., Li, F., Zheng, H. T., Jia,  
830 G. L., Lu, M. M., Wu, L., and Carmichael, G. R.: A 6-year-long (2013-2018) high-  
831 resolution air quality reanalysis dataset in China based on the assimilation of surface  
832 observations from CNEMC, Earth System Science Data, 13, 529-570,  
833 <https://doi.org/10.5194/essd-13-529-2021>, 2021.

834 Kuniyal, J. C. and Guleria, R. P.: The current state of aerosol-radiation interactions: A mini  
835 review, Journal of Aerosol Science, 130, 45-54,  
836 <https://doi.org/10.1016/j.jaerosci.2018.12.010>, 2019.

837 Lan, X.: Atmospheric Carbon Dioxide Dry Air Mole Fractions from the NOAA GML Carbon  
838 Cycle Cooperative Global Air Sampling Network, 1968-2022, Version: 2023-08-28, [data  
839 set], <https://doi.org/10.15138/wkgj-f215>, 2023.

840 Lawrence, P. J. and Chase, T. N.: Representing a new MODIS consistent land surface in the  
841 Community Land Model (CLM 3.0), J. Geophys. Res.: Biogeosci., 112, G01023,  
842 <https://doi.org/10.1029/2006jg000168>, 2007.

843 Lei, Y., Yue, X., Wang, Z., Liao, H., Zhang, L., Tian, C., Zhou, H., Zhong, J., Guo, L., Che, H.,  
844 and Zhang, X.: Mitigating ozone damage to ecosystem productivity through sectoral and  
845 regional emission controls: a case study in the Yangtze River Delta, China, Environmental  
846 Research Letters, 17, <https://doi.org/10.1088/1748-9326/ac6ff7>, 2022.

847 Levy, R. C., Mattoe, S., Munchak, L. A., Remer, L. A., Sayer, A. M., Patadia, F., and Hsu, N.  
848 C.: The Collection 6 MODIS aerosol products over land and ocean, Atmospheric  
849 Measurement Techniques, 6, 2989-3034, <https://doi.org/10.5194/amt-6-2989-2013>, 2013.

850 Li, M., Huang, X., Yan, D., Lai, S., Zhang, Z., Zhu, L., Lu, Y., Jiang, X., Wang, N., Wang, T.,  
851 Song, Y., and Ding, A.: Coping with the concurrent heatwaves and ozone extremes in  
852 China under a warming climate, Science Bulletin, 69, 2938-2947,  
853 <https://doi.org/10.1016/j.scib.2024.05.034>, 2024.

854 Li, M., Liu, H., Geng, G. N., Hong, C. P., Liu, F., Song, Y., Tong, D., Zheng, B., Cui, H. Y.,  
855 Man, H. Y., Zhang, Q., and He, K. B.: Anthropogenic emission inventories in China: a  
856 review, National Science Review, 4, 834-866, <https://doi.org/10.1093/nsr/nwx150>, 2017.

857 Li, X., Liang, H., and Cheng, W.: Spatio-Temporal Variation in AOD and Correlation Analysis



858 with PAR and NPP in China from 2001 to 2017, *Remote Sens.*, 12,  
859 <https://doi.org/10.3390/rs12060976>, 2020.

860 Liu, H., Liu, S., Xue, B., Lv, Z., Meng, Z., Yang, X., Xue, T., Yu, Q., and He, K.: Ground-level  
861 ozone pollution and its health impacts in China, *Atmos. Environ.*, 173, 223-230,  
862 <https://doi.org/10.1016/j.atmosenv.2017.11.014>, 2018.

863 Liu, L., Wen, Z., Liu, S., Zhang, X., and Liu, X.: Decline in atmospheric nitrogen deposition  
864 in China between 2010 and 2020, *Nature Geoscience*, 17, <https://doi.org/10.1038/s41561-024-01484-4>, 2024.

865 Liu, M., Shang, F., Lu, X., Huang, X., Song, Y., Liu, B., Zhang, Q., Liu, X., Cao, J., Xu, T.,  
866 Wang, T., Xu, Z., Xu, W., Liao, W., Kang, L., Cai, X., Zhang, H., Dai, Y., and Zhu, T.:  
867 Unexpected response of nitrogen deposition to nitrogen oxide controls and implications  
868 for land carbon sink, *Nature Communications*, 13, <https://doi.org/10.1038/s41467-022-30854-y>, 2022.

869 Liu, X., Zhang, Y., Han, W., Tang, A., Shen, J., Cui, Z., Vitousek, P., Erisman, J. W., Goulding,  
870 K., Christie, P., Fangmeier, A., and Zhang, F.: Enhanced nitrogen deposition over China,  
871 *Nature*, 494, 459-462, <https://doi.org/10.1038/nature11917>, 2013.

872 Lu, X., Hou, E., Guo, J., Gilliam, F. S., Li, J., Tang, S., and Kuang, Y.: Nitrogen addition  
873 stimulates soil aggregation and enhances carbon storage in terrestrial ecosystems of China:  
874 A meta-analysis, *Global Change Biology*, 27, 2780-2792,  
875 <https://doi.org/10.1111/gcb.15604>, 2021.

876 Lu, X., Jiang, H., Liu, J., Zhang, X., Jin, J., Zhu, Q., Zhang, Z., and Peng, C.: Simulated effects  
877 of nitrogen saturation on the global carbon budget using the IBIS model, *Sci. Rep.*, 6,  
878 <https://doi.org/10.1038/srep39173>, 2016.

879 Lu, X., Zhang, L., Wang, X. L., Gao, M., Li, K., Zhang, Y. Z., Yue, X., and Zhang, Y. H.: Rapid  
880 Increases in Warm-Season Surface Ozone and Resulting Health Impact in China Since  
881 2013, *Environmental Science & Technology Letters*, 7, 240-247,  
882 <https://doi.org/10.1021/acs.estlett.0c00171>, 2020.

883 Luo, Y. X., Zheng, X. B., Zhao, T. L., and Chen, J.: A climatology of aerosol optical depth over  
884 China from recent 10 years of MODIS remote sensing data, *IJCLI*, 34, 863-870,



887 https://doi.org/10.1002/joc.3728, 2014.

888 Ma, D. Y., Wang, T. J., Wu, H., Qu, Y. W., Liu, J., Liu, J. E., Li, S., Zhuang, B. L., Li, M. M.,  
889 and Xie, M.: The effect of anthropogenic emission, meteorological factors, and  
890 carbondioxide on the surface ozone increase in China from 2008 to 2018 during the East  
891 Asia summer monsoon season, *Atmos. Chem. Phys.*, 23, 6525-6544,  
892 https://doi.org/10.5194/acp-23-6525-2023, 2023.

893 Madani, N., Kimball, J. S., Affleck, D. L. R., Kattge, J., Graham, J., van Bodegom, P. M., Reich,  
894 P. B., and Running, S. W.: Improving ecosystem productivity modeling through spatially  
895 explicit estimation of optimal light use efficiency, *J. Geophys. Res.: Biogeosci.*, 119,  
896 1755-1769, https://doi.org/10.1002/2014jg002709, 2014.

897 Mercado, L. M., Bellouin, N., Sitch, S., Boucher, O., Huntingford, C., Wild, M., and Cox, P.  
898 M.: Impact of changes in diffuse radiation on the global land carbon sink, *Nature*, 458,  
899 1014-U1087, https://doi.org/10.1038/nature07949, 2009.

900 Oliphant, A. J., Dragoni, D., Deng, B., Grimmond, C. S. B., Schmid, H. P., and Scott, S. L.:  
901 The role of sky conditions on gross primary production in a mixed deciduous forest, *Agric.  
902 For. Meteorol.*, 151, 781-791, https://doi.org/10.1016/j.agrformet.2011.01.005, 2011.

903 Peng, X., Wei, W., Niu, S., Huang, Y., and Chen, L.: Divergent impact of long-term  
904 anthropogenic nitrogen inputs on global particulate and mineral-associated organic carbon,  
905 *Ecological Processes*, 14, https://doi.org/10.1186/s13717-025-00624-x, 2025.

906 Peters, W., Jacobson, A. R., Sweeney, C., Andrews, A. E., Conway, T. J., Masarie, K., Miller,  
907 J. B., Bruhwiler, L. M. P., Petron, G., Hirsch, A. I., Worthy, D. E. J., van der Werf, G. R.,  
908 Randerson, J. T., Wennberg, P. O., Krol, M. C., and Tans, P. P.: An atmospheric perspective  
909 on North American carbon dioxide exchange: CarbonTracker, *Proc. Natl. Acad. Sci.  
910 U.S.A.*, 104, 18925-18930, https://doi.org/10.1073/pnas.0708986104, 2007.

911 Piao, S., He, Y., Wang, X., and Chen, F.: Estimation of China's terrestrial ecosystem carbon  
912 sink: Methods, progress and prospects, *Science China Earth Sciences*, 65, 641-651,  
913 https://doi.org/10.1007/s11430-021-9892-6, 2022.

914 Piao, S., Sitch, S., Ciais, P., Friedlingstein, P., Peylin, P., Wang, X., Ahlstrom, A., Anav, A.,  
915 Canadell, J. G., Cong, N., Huntingford, C., Jung, M., Levis, S., Levy, P. E., Li, J., Lin, X.,



916 Lomas, M. R., Lu, M., Luo, Y., Ma, Y., Myneni, R. B., Poulter, B., Sun, Z., Wang, T.,  
917 Viovy, N., Zaehle, S., and Zeng, N.: Evaluation of terrestrial carbon cycle models for their  
918 response to climate variability and to CO<sub>2</sub> trends, *Glob. Chang. Biol.*, 19, 2117-2132,  
919 <https://doi.org/10.1111/gcb.12187>, 2013.

920 Platnick, S., King, M., and Hubanks, P.: MOD08\_M3 - MODIS/Terra Aerosol Cloud Water  
921 Vapor Ozone Monthly L3 Global 1Deg CMG, NASA MODIS Adaptive Processing  
922 System, Goddard Space Flight Center [data set], USA,  
923 [https://doi.org/10.5067/MODIS/MOD08\\_M3.061](https://doi.org/10.5067/MODIS/MOD08_M3.061), 2015.

924 Post, E., Steinman, B. A., and Mann, M. E.: Acceleration of phenological advance and warming  
925 with latitude over the past century, *Sci. Rep.*, 8, 3927, [https://doi.org/10.1038/s41598-018-22258-0](https://doi.org/10.1038/s41598-018-<br/>926 22258-0), 2018.

927 Ren, W., Tian, H. Q., Tao, B., Huang, Y., and Pan, S. F.: China's crop productivity and soil  
928 carbon storage as influenced by multifactor global change, *Global Change Biology*, 18,  
929 2945-2957, <https://doi.org/10.1111/j.1365-2486.2012.02741.x>, 2012.

930 Ren, W., Banger, K., Tao, B., Yang, J., Huang, Y., and Tian, H.: Global pattern and change of  
931 cropland soil organic carbon during 1901-2010: Roles of climate, atmospheric chemistry,  
932 land use and management, *Geography and Sustainability*, 1, 59-69,  
933 <https://doi.org/10.1016/j.geosus.2020.03.001>, 2020.

934 Running, S., Mu, Q., Zhao, M.: MOD17A2H MODIS/Terra Gross Primary Productivity 8-Day  
935 L4 Global 500m SIN Grid V006, NASA EOSDIS Land Processes Distributed Active  
936 Archive Center, [data set], <https://doi.org/10.5067/MODIS/MOD17A2H.006>, 2015.

937 Shalaby, A., Zakey, A. S., Tawfik, A. B., Solomon, F., Giorgi, F., Stordal, F., Sillman, S., Zaveri,  
938 R. A., and Steiner, A. L.: Implementation and evaluation of online gas-phase chemistry  
939 within a regional climate model (RegCM-CHEM4), *Geosci. Model Dev.*, 5, 741-760,  
940 <https://doi.org/10.5194/gmd-5-741-2012>, 2012.

941 Shang, F., Liu, M. X., Song, Y., Lu, X. J., Zhang, Q., Matsui, H., Liu, L. L., Ding, A. J., Huang,  
942 X., Liu, X. J., Cao, J. J., Wang, Z. F., Dai, Y. J., Kang, L., Cai, X. H., Zhang, H. S., and  
943 Zhu, T.: Substantial nitrogen abatement accompanying decarbonization suppresses  
944 terrestrial carbon sinks in China, *Nature Communications*, 15,



945 https://doi.org/10.1038/s41467-024-52152-5, 2024.

946 Shu, Y., Liu, S., Wang, Z., Xiao, J., Shi, Y., Peng, X., Gao, H., Wang, Y., Yuan, W., Yan, W.,  
947 Ning, Y., and Li, Q.: Effects of Aerosols on Gross Primary Production from Ecosystems  
948 to the Globe, *Remote Sens.*, 14, <https://doi.org/10.3390/rs14122759>, 2022.

949 Sitch, S., Cox, P. M., Collins, W. J., and Huntingford, C.: Indirect radiative forcing of climate  
950 change through ozone effects on the land-carbon sink, *Nature*, 448, 791-U794,  
951 <https://doi.org/10.1038/nature06059>, 2007.

952 Strada, S. and Unger, N.: Potential sensitivity of photosynthesis and isoprene emission to direct  
953 radiative effects of atmospheric aerosol pollution, *Atmos. Chem. Phys.*, 16, 4213-4234,  
954 <https://doi.org/10.5194/acp-16-4213-2016>, 2016.

955 Tang, M. J., Huang, X., Lu, K. D., Ge, M. F., Li, Y. J., Cheng, P., Zhu, T., Ding, A. J., Zhang,  
956 Y. H., Gligorovski, S., Song, W., Ding, X., Bi, X. H., and Wang, X. M.: Heterogeneous  
957 reactions of mineral dust aerosol: implications for tropospheric oxidation capacity, *Atmos.*  
958 *Chem. Phys.*, 17, 11727-11777, <https://doi.org/10.5194/acp-17-11727-2017>, 2017.

959 Tu, M., Liu, Z., He, C., Fang, Z., and Lu, W.: The relationships between urban landscape  
960 patterns and fine particulate pollution in China: A multiscale investigation using a  
961 geographically weighted regression model, *Journal of Cleaner Production*, 237,  
962 <https://doi.org/10.1016/j.jclepro.2019.117744>, 2019.

963 Unger, N., Yue, X., and Harper, K. L.: Aerosol climate change effects on land ecosystem  
964 services, *Faraday Discuss.*, 200, 121-142, <https://doi.org/10.1039/c7fd00033b>, 2017.

965 Unger, N., Zheng, Y., Yue, X., and Harper, K. L.: Mitigation of ozone damage to the world's  
966 land ecosystems by source sector, *Nature Climate Change*, 10, 134-+,  
967 <https://doi.org/10.1038/s41558-019-0678-3>, 2020.

968 Wang, J., Dong, J., Yi, Y., Lu, G., Oyler, J., Smith, W. K., Zhao, M., Liu, J., and Running, S.:  
969 Decreasing net primary production due to drought and slight decreases in solar radiation  
970 in China from 2000 to 2012, *J. Geophys. Res.: Biogeosci.*, 122, 261-278,  
971 <https://doi.org/10.1002/2016jg003417>, 2017.

972 Wang, K., Zhang, Y., Yahya, K., Wu, S. Y., and Grell, G.: Implementation and initial application  
973 of new chemistry-aerosol options in WRF/Chem for simulating secondary organic



974 aerosols and aerosol indirect effects for regional air quality, *Atmos. Environ.*, 115, 716-  
975 732, <https://doi.org/10.1016/j.atmosenv.2014.12.007>, 2015.

976 Wang, X., Wu, J., Chen, M., Xu, X., Wang, Z., Wang, B., Wang, C., Piao, S., Lin, W., Miao,  
977 G., Deng, M., Qiao, C., Wang, J., Xu, S., and Liu, L.: Field evidences for the positive  
978 effects of aerosols on tree growth, *Global Change Biology*, 24, 4983-4992,  
979 <https://doi.org/10.1111/gcb.14339>, 2018.

980 Wang, Y., Ni, J., Xu, K., Zhang, H., Gong, X., and He, C.: Intricate synergistic effects between  
981 air pollution and carbon emission: An emerging evidence from China, *Environ. Pollut.*,  
982 349, <https://doi.org/10.1016/j.envpol.2024.123851>, 2024.

983 Wittig, V. E., Ainsworth, E. A., and Long, S. P.: To what extent do current and projected  
984 increases in surface ozone affect photosynthesis and stomatal conductance of trees? A  
985 meta-analytic review of the last 3 decades of experiments, *Plant Cell and Environment*,  
986 30, 1150-1162, <https://doi.org/10.1111/j.1365-3040.2007.01717.x>, 2007.

987 Xia, J., Xia, X., Wang, X., Ju, W., Lin, Z., Qin, Z., Sang, Y., Yan, Y., Yuan, W., Yue, X., Zhang,  
988 H., Zhou, H., and Zhu, Q.: China Land Carbon Budget (CLCB1.0): a comprehensive  
989 estimate of the land carbon budget in China, *National Science Review*, 12,  
990 <https://doi.org/10.1093/nsr/nwaf052>, 2025.

991 Xie, N., Wang, T., Xie, X., Yue, X., Giorgi, F., Zhang, Q., Ma, D., Song, R., Xu, B., Li, S.,  
992 Zhuang, B., Li, M., Xie, M., Kilifarska, N. A., Gadzhev, G., and Dimitrova, R.: The  
993 regional climate-chemistry-ecology coupling model RegCM-Chem (v4.6)-YIBs (v1.0):  
994 development and application, *Geosci. Model Dev.*, 17, 3259-3277,  
995 <https://doi.org/10.5194/gmd-17-3259-2024>, 2024.

996 Xie, N. H., Wang, T. J., Xie, M., Ma, D. Y., Zhang, Q., Li, M. M., Li, S., Zhuang, B. L., Kalsoom,  
997 U., Kilifarska, N. A., Gadzhev, G., Dimitrova, R., Melas, D., and Karatzas, K.: Carbon  
998 Sink of Terrestrial Ecosystems in China During 2010-2020: Spatiotemporal Variability  
999 and Climate Impact, *J. Geophys. Res.: Atmos.*, 130,  
1000 <https://doi.org/10.1029/2025jd043405>, 2025.

1001 Xie, X., Wang, T., Yue, X., Li, S., Zhuang, B., and Wang, M.: Effects of atmospheric aerosols  
1002 on terrestrial carbon fluxes and CO<sub>2</sub> concentrations in China, *Atmos. Res.*,



1003 237, <https://doi.org/10.1016/j.atmosres.2020.104859>, 2020.

1004 1004 Xie, X. D., Wang, T. J., Yue, X., Li, S., Zhuang, B. L., Wang, M. H., and Yang, X. Q.: Numerical  
1005 modeling of ozone damage to plants and its effects on atmospheric CO<sub>2</sub> in China, *Atmos.*  
1006 *Environ.*, 217, 116970, <https://doi.org/10.1016/j.atmosenv.2019.116970>, 2019.

1007 1007 Xue, T., Liu, J., Zhang, Q., Geng, G., Zheng, Y., Tong, D., Liu, Z., Guan, D., Bo, Y., Zhu, T.,  
1008 He, K., and Hao, J.: Rapid improvement of PM<sub>2.5</sub> pollution and associated  
1009 health benefits in China during 2013-2017, *Science China-Earth Sciences*, 62, 1847-1856,  
1010 <https://doi.org/10.1007/s11430-018-9348-2>, 2019.

1011 1011 Yan, S. Q., Zhu, B., Shi, S. S., Lu, W., Gao, J. H., Kang, H. Q., and Liu, D. Y.: Impact of aerosol  
1012 optics on vertical distribution of ozone in autumn over Yangtze River Delta, *Atmos. Chem.*  
1013 *Phys.*, 23, 5177-5190, <https://doi.org/10.5194/acp-23-5177-2023>, 2023.

1014 1014 Yang, H., Chen, L., Liao, H., Zhu, J., Wang, W. J., and Li, X.: Impacts of aerosol-photolysis  
1015 interaction and aerosol-radiation feedback on surface-layer ozone in North China during  
1016 multi-pollutant air pollution episodes, *Atmos. Chem. Phys.*, 22, 4101-4116,  
1017 <https://doi.org/10.5194/acp-22-4101-2022>, 2022.

1018 1018 Yu, G., Jia, Y., He, N., Zhu, J., Chen, Z., Wang, Q., Piao, S., Liu, X., He, H., Guo, X., Wen, Z.,  
1019 Li, P., Ding, G., and Goulding, K.: Stabilization of atmospheric nitrogen deposition in  
1020 China over the past decade, *Nature Geoscience*, 12, 424+,  
1021 <https://doi.org/10.1038/s41561-019-0352-4>, 2019.

1022 1022 Yuan, X., Chen, X., Ochege, F. U., Hamdi, R., Tabari, H., Li, B., He, B., Zhang, C., De Maejer,  
1023 P., and Luo, G.: Weakening of global terrestrial carbon sequestration capacity under  
1024 increasing intensity of warm extremes, *Nature Ecology & Evolution*, 9,  
1025 <https://doi.org/10.1038/s41559-024-02576-5>, 2025.

1026 1026 Yue, H., He, C., Huang, Q., Yin, D., and Bryan, B. A.: Stronger policy required to substantially  
1027 reduce deaths from PM<sub>2.5</sub> pollution in China, *Nature Communications*, 11,  
1028 <https://doi.org/10.1038/s41467-020-15319-4>, 2020.

1029 1029 Yue, K., Peng, Y., Peng, C., Yang, W., Peng, X., and Wu, F.: Stimulation of terrestrial ecosystem  
1030 carbon storage by nitrogen addition: a meta-analysis, *Sci. Rep.*, 6,  
1031 <https://doi.org/10.1038/srep19895>, 2016.



1032 Yue, X. and Unger, N.: The Yale Interactive terrestrial Biosphere model version 1.0: description,  
1033 evaluation and implementation into NASA GISS ModelE2, *Geosci. Model Dev.*, 8, 2399-  
1034 2417, <https://doi.org/10.5194/gmd-8-2399-2015>, 2015.

1035 Yue, X. and Unger, N.: Aerosol optical depth thresholds as a tool to assess diffuse radiation  
1036 fertilization of the land carbon uptake in China, *Atmos. Chem. Phys.*, 17, 1329-1342,  
1037 <https://doi.org/10.5194/acp-17-1329-2017>, 2017.

1038 Yue, X., Zhang, T., and Shao, C.: Afforestation increases ecosystem productivity and carbon  
1039 storage in China during the 2000s, *Agric. For. Meteorol.*, 296, 108227,  
1040 <https://doi.org/10.1016/j.agrformet.2020.108227>, 2021.

1041 Yue, X., Unger, N., Harper, K., Xia, X., Liao, H., Zhu, T., Xiao, J., Feng, Z., and Li, J.: Ozone  
1042 and haze pollution weakens net primary productivity in China, *Atmos. Chem. Phys.*, 17,  
1043 6073-6089, <https://doi.org/10.5194/acp-17-6073-2017>, 2017.

1044 Zhang, F. M., Chen, J. M., Chen, J. Q., Gough, C. M., Martin, T. A., and Dragoni, D.:  
1045 Evaluating spatial and temporal patterns of MODIS GPP over the conterminous US  
1046 against flux measurements and a process model, *Remote Sensing of Environment*, 124,  
1047 717-729, <https://doi.org/10.1016/j.rse.2012.06.023>, 2012.

1048 Zhang, Q., Wang, T. J., Wu, H., Qu, Y. W., Xie, M., Li, S., Zhuang, B. L., Li, M. M., and  
1049 Kilifarska, N. A.: Radiative and Chemical Effects of Non-Homogeneous Methane on  
1050 Terrestrial Carbon Fluxes in Asia, *J. Geophys. Res.: Atmos.*, 129,  
1051 <https://doi.org/10.1029/2023jd040204>, 2024.

1052 Zhang, Q., Wang, T., Zhang, Z., Xu, X., Xie, N., Zhuang, B., Li, S., Gao, L., Li, M., and Xie,  
1053 M.: Methane Emissions in Asian Wetlands During 2010–2020: Insights From an Online-  
1054 Coupled Microbial Functional-Group-Based Model, *Earth's Future*, 13,  
1055 <https://doi.org/10.1029/2025ef005991>, 2025.

1056 Zhang, W. W., Wang, M., Wang, A. Y., Yin, X. H., Feng, Z. Z., and Hao, G. Y.: Elevated ozone  
1057 concentration decreases whole-plant hydraulic conductance and disturbs water use  
1058 regulation in soybean plants, *Physiologia Plantarum*, 163, 183-195,  
1059 <https://doi.org/10.1111/ppl.12673>, 2018.

1060 Zheng, B., Tong, D., Li, M., Liu, F., Hong, C. P., Geng, G. N., Li, H. Y., Li, X., Peng, L. Q., Qi,



1061 J., Yan, L., Zhang, Y. X., Zhao, H. Y., Zheng, Y. X., He, K. B., and Zhang, Q.: Trends in  
1062 China's anthropogenic emissions since 2010 as the consequence of clean air actions,  
1063 *Atmos. Chem. Phys.*, 18, 14095-14111, <https://doi.org/10.5194/acp-18-14095-2018>, 2018.

1064 Zhou, H., Yue, X., Lei, Y., Tian, C., Ma, Y., and Cao, Y.: Aerosol radiative and climatic effects  
1065 on ecosystem productivity and evapotranspiration, *Current Opinion in Environmental  
1066 Science & Health*, 19, <https://doi.org/10.1016/j.coesh.2020.10.006>, 2021.

1067 Zhou, H., Yue, X., Lei, Y., Tian, C., Zhu, J., Ma, Y., Cao, Y., Yin, X., and Zhang, Z.:  
1068 Distinguishing the impacts of natural and anthropogenic aerosols on global gross primary  
1069 productivity through diffuse fertilization effect, *Atmos. Chem. Phys.*, 22, 693-709,  
1070 <https://doi.org/10.5194/acp-22-693-2022>, 2022.

1071 Zhou, H., Yue, X., Dai, H., Geng, G., Yuan, W., Chen, J., Shen, G., Zhang, T., Zhu, J., and Liao,  
1072 H.: Recovery of ecosystem productivity in China due to the Clean Air Action plan, *Nature  
1073 Geoscience*, 17, <https://doi.org/10.1038/s41561-024-01586-z>, 2024.

1074 Zhu, J. X., Jia, Y. L., Yu, G. R., Wang, Q. F., He, N. P., Chen, Z., He, H. L., Zhu, X. J., Li, P.,  
1075 Zhang, F. S., Liu, X. J., Goulding, K., Fowler, D., and Vitousek, P.: Changing patterns of  
1076 global nitrogen deposition driven by socio-economic development, *Nature  
1077 Communications*, 16, <https://doi.org/10.1038/s41467-024-55606-y>, 2025.

1078  
1079